Utrecht University

Master Thesis Bas Salzmann

Towards luminescent temperature sensing in catalytic environments by exploiting $Y_2O_3:Ln^{3+}$ / α-Al_2O_3 complexes

Supervisors:
Robin Geitenbeek
Anne-Eva Nieuwelink
Andries Meijerink
Bert Weckhuysen

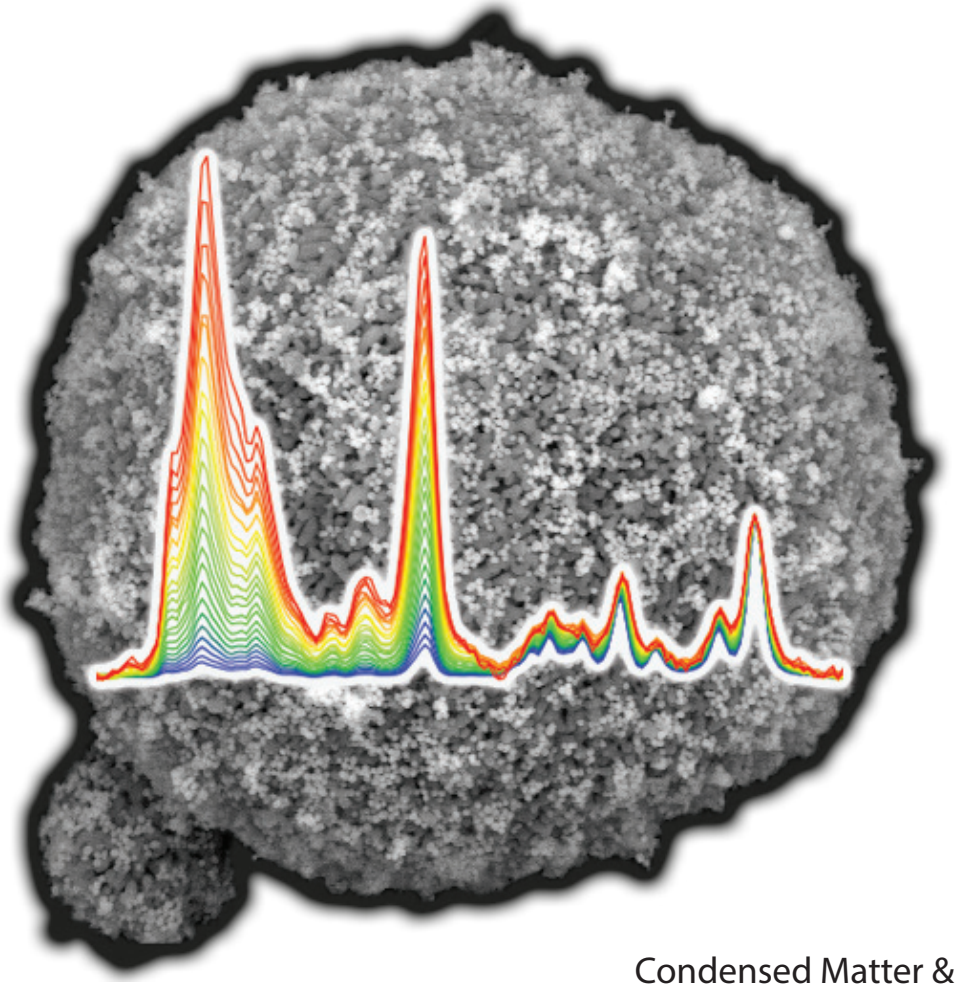

February 2017
Condensed Matter & Interfaces and
Inorganic Chemistry & Catalysis
Utrecht University

Cover image: artist's impression of a SEM image of lanthanide-doped Y_2O_3 NPs deposited on α-Al_2O_3, combined with temperature dependent emission spectra of Er^{3+}/Yb^{3+}-doped complexes.

Abstract

Temperature is an important parameter in catalysis since it is related to the yield, selectivity and reaction speed of chemical conversions. Currently, it is not feasible to determine the temperature of industrial reactors *in situ* with a high spatial and thermal resolution. This is a major drawback for the control and optimization of the temperature in reactors.

Here, we report the synthesis of Y_2O_3:Ln NPs (Ln = Eu^{3+}, Dy^{3+} or Er^{3+}/Yb^{3+}) / α-Al_2O_3 temperature probes for *in situ* temperature determination in catalytic reactors with a high spatial and thermal resolution. Y_2O_3:Ln NPs synthesized by homogenous precipitation are between 50 and 250 nm in size and were deposited on the α-Al_2O_3 support material. Thermal and mechanical stability experiments confirmed firm adhesion of the NPs on α-Al_2O_3 and thermal stability of the complexes up to 600 ºC. Temperature dependent emission was observed for Eu^{3+}- and Er^{3+}/Yb^{3+}-doped complexes for the temperature regions of 225-600 ºC and 22-500 ºC with accuracies higher than 14 and 3 ºC, respectively. Although the Dy^{3+}-doped complexes exhibited temperature dependent luminescence, the signal to noise ratio was unsufficient for temperature determination. Thermal cycling experiments up to 600 ºC confirmed the preservation of luminescence after multiple cycles. Further research is required to study the temperature probes under industrially relevant conditions.

Contents

Chapter 1 - Introduction

1.1 Catalysis and temperature probing

Catalysis is an important field in the production of chemicals. Estimated is that for 85-90 % of the industrial chemicals a catalyst is used in the production.[1] A catalyst speeds up the reaction by the reduction of the activation energy ΔE as shown in Figure 1-1. The decrease of the activation energy leads to an increase in the reaction rate k since it is coupled with the activation energy ΔE in the well-known Arrhenius equation: $k = Ae^{-\Delta E / kT}$.

Most chemical reactions are thermally activated and thus strongly depend on the temperature during reaction.[2] Yield and selectivity are related to the temperature which is in most cases inhomogeneously distributed over a reactor. The temperature distribution leads to unwanted by-products and/or a lower yield.[2] Furthermore, non-optimal temperatures lower the Currently, the temperature of chemical reactors is measured by infrared thermography and/or thermocouples and resistance temperature detectors.[3]

The first method, infrared tomography, is based on the determination of the temperature from thermal radiance. However, this method is only capable of determining the surface temperature of a reactor and takes the interior not into account.[3] The determined temperature deviates strongly from the actual temperature in the reactor since the chemical conversions take place in the center of the reactor. Figure 1-2 (a) shows an example where the temperature of the surface of a reactor is visualized. Cold surfaces appear purple whereas hot surfaces appear yellow.

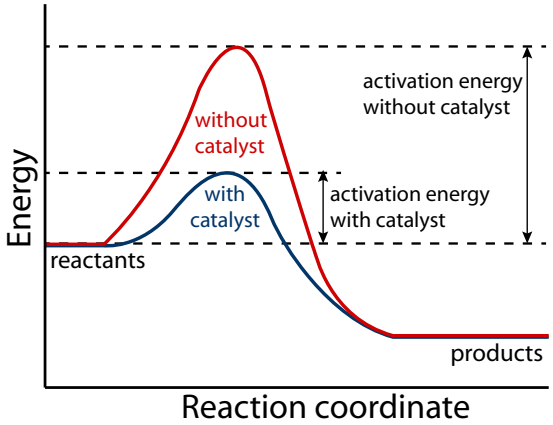

Figure 1-1: Energy diagram of a catalytic reaction with and without catalyst. The activation energy of the reaction is lowered by the addition of the catalyst, resulting in an increase of the speed of the reaction.

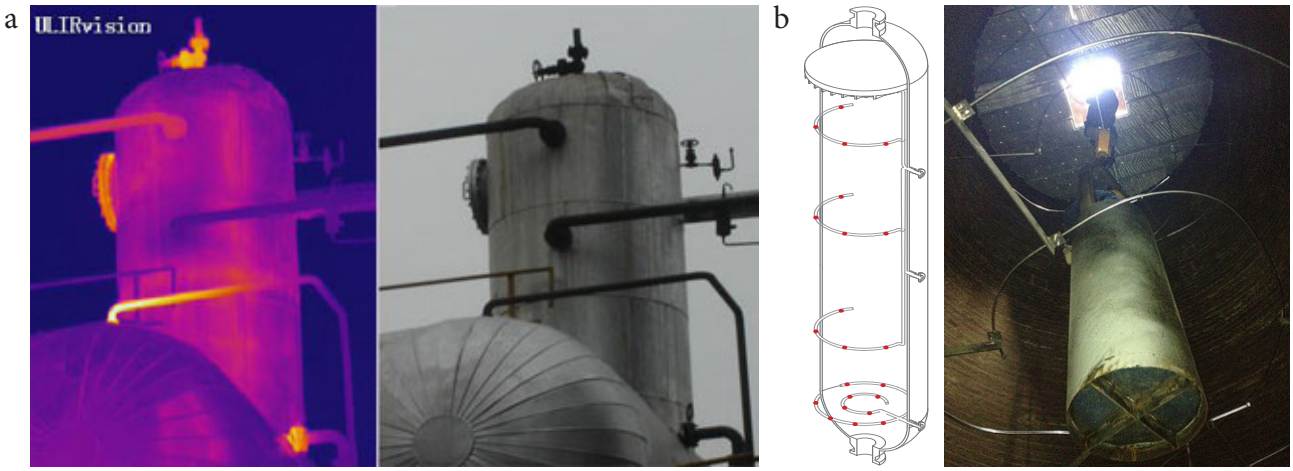

Figure 1-2: Two methods for determing the temperature of industrial reactors: (a) infrared thermography and (b) thermocouple and/or resistance sensors. (a): temperature distribution imaged of a chemical reactor with infrared thermography. Cold regions appear purple whereas hot regions appear yellow. Images from http://www.ulirvision.co.uk/application-details-2.html and http://www.dailyinst.com/reactor-thermometry.html, respectively.

The second method, measurements with thermocouples and/or resistance sensors, is shown in Figure 1-2 (b). Spirals made from steel, containing the sensors which are depicted as red dots, are placed in the reactor at different stages, resulting in the determination of temperature *in situ*. Nevertheless, the probing resolution is low, *i.e.* the temperatures are measured over a relatively large volume in which temperature fluctuations on small scale are not taken into account.

Since the present techniques are unable to probe the temperature in chemical reactors *in situ* with a high spatial and temporal resolution, there is a need for a new probing technique.

1.2 Nanothermometry

An emerging new field in nanoscience is nanothermometry. This field aims to extract information about temperature on a very small spatial scale, *e.g.* the sub-micrometer regime. Nanothermometry is currently exploited in micro- and nano-electronics[4,5], integrated photonics[6] and biomedicine[7]. In all these fields a high spatial resolution is needed to optimize or control processes. To do this, one needs such small thermometers on such small length scale. Various nanothermometers are being developed which are based on electrical, mechanical or optical techniques.[8]

Electrical and mechanical probing techniques are based on the variation of resistance, voltage, conductivity, electrical capacity or mechanical bending of temperature probes.[9,10] Although these techniques are able to obtain a high spatial and thermal resolution, they lack the capability of handling large areas and require contact between the probe and system under study, leading to temperature deviations. Furthermore, these nanothermometers are not applicable for chemical reactors. Therefore, these methods are unsuitable for temperature probing in catalysis.

Optical nanothermometry solves these shortcomings by probing the temperature non-invasively using luminescent materials. The thermal reading is performed by measuring the temperature dependent spectral position, bandwith, intensity, polarization, or lifetime of emission.[8] So far, various materials have been discovered which exhibit these features and are grouped into four classes: quantum dots (QDs), dye-based organic compounds, polymers and lanthanides.

The first class, QDs, are made of semiconducting materials and show temperature dependent emission by a decrease in emission intensity and a shift to lower energies.[11,12] However, QDs are generally unstable under normal atmosphere and the emission intensity strongly decreases above room temperature which makes the usage as temperature probes inappropriate. The second and third class, dye-based organic compounds and polymers are made of organic materials and exhibit temperature dependent luminescence from the emission of higher electronic states.[13,14] However, the luminescence of both systems is strongly coupled to the properties of the environment (*e.g.* pH, solvent and concentration of luminescent centers). Furthermore, the materials decompose at high temperatures which makes them unsuitable for catalytic environments.

The fourth class, lanthanides, is a promising candidate for temperature probing in catalytic environments. Lanthanides exhibit sharp and environment-independent luminescence and show high thermal quenching temperatures. Kusuma proposed in 1976 that if the energy difference between two adjacent energy levels smaller than several k_BT, the populations are thermally coupled, resulting in temperature dependent emission.[15] Consequently, the temperature can be determined from the fluorescence intensity ratio of the thermally coupled emission. This method is favourable over other methods (*e.g.* determination via the spectral bandwith or lifetime), since it is independent of sample variations such as concentration, excitation power or re-alignments of the set-up.

Until now, numerous studies have been performed on the temperature dependent luminescence of lanthanides in a variety of (co-)doped host materials. Temperature probing has successfully been exploited in organic host materials with workable ranges up to 200 ºC.[16] However, these organic host materials decompose at higher temperatures and are therefore unsuitable for temperature probing in catalytic environments. On the contrary, inorganic hosts such as Gd_2O_3, YAG ($Y_3Al_5O_{12}$) and Y_2O_3

have shown to exhibit temperature dependent luminescence up 800 ºC.[17-19] These host materials could easily be doped with luminescent lanthanide ions such as Eu^{3+}, Dy^{3+}, Er^{3+} and Yb^{3+}. Furthermore, these materials exhibit low phonon energies and higher chemical stability which makes the usage favourable.

In this work, we investigated the temperature dependent luminescence of Y_2O_3:Ln NPs (Ln = Eu^{3+}, Dy^{3+} or Er^{3+}/Yb^{3+}) on α-Al_2O_3, relevant for thermometry in chemical reactors up to 600 °C. The complexes were made by the deposition of Y_2O_3:Ln NPs on the catalytic support material α-Al_2O_3. The deposition of the Ln-doped Y_2O_3 NPs on α-Al_2O_3 yielded thermally and mechanically stable complexes that were tested for behaviour in temperature dependent luminescence.

It was found that Y_2O_3:$Eu_{0.05}$ NPs / α-Al_2O_3 complexes exhibited temperature dependent emission between 225 and 600 °C. We were not able to deduce a temperature dependence from Y_2O_3:$Dy_{0.0085}$ NPs / α-Al_2O_3 because the signal to noise ratio was unsufficient. Upconversion luminescence of Y_2O_3:$Er_{0.01}Yb_{0.01}$ NPs / α-Al_2O_3 complexes revealed the presence of temperature dependent luminescence from room temperature up to 500 °C. Thermal cycling experiments were carried out to investigate the durability and accuracy of the temperature probes. All systems have shown to remain their luminescence during the thermal cycles. The accuracy was relatively low, between 5.0 and 14.2 °C, for the Y_2O_3:$Eu_{0.05}$ NPs / α-Al_2O_3 since the complexes exhibited low emission intensity at elevated temperatures. However, the Y_2O_3:$Er_{0.01}Yb_{0.01}$ NPs / α-Al_2O_3 showed a higher accuracy between 0.7 and 2.8 °C because of a higher emission intensity and larger change in luminescence ratio.

1.3 References

[1] I. Chorkendorff and J.W. Niemantsverdriet. Concepts of modern catalysis and kinetics. *Wiley-VCH*, 2003.

[2] E.B. Nauman, Chemical reactor design, optimization, and scaleup. *McGraw-Hill*, 2002.

[3] S. Bagavathiappan, B. B. Lahiri, T. Saravanan, J. Philip and T. Jayakumar. Infrared thermography for condition monitoring - A review. *Infrared Physics and Technology*, 60:35-55, 2013.

[4] L. Aigouy, G. Tessier, M. Mortier and B. Charlot. Scanning thermal imaging of microelectronic circuits with a fluorescent nanoprobe. *Applied Physics Letter*, 87:184105, 2005.

[5] A. Zimmers, L. Aigouy, M. Mortier, A. Sharoni, S. Wang, K.G. West, J.G. Ramirez and I.K. Schuller. Role of thermal heating on the voltage induced insulator-metal transition in VO_2. *Physical Review Letters*, 110:056601, 2013.

[6] G. Nenna, G. Flaminio, T. Fasolino, C. Minarini, R. Miscioscia, D. Palumbo and M. Pellegrino. A study on thermal degradation of organic LEDs using IR imaging. *Macromolecular Symposia*, 247:326-332, 2007.

[7] D. Jaque, B. del Rosal, E.M. Rodríguez, L.M. Maestro, P. Haro-González and J.G. Solé. Fluorescent nanothermometers for intracellular thermal sensing. *Nanomedicine*, 9:1047-1062, 2014.

[8] D. Jaque and F. Vetrone. Luminescence nanothermometry. *Nanoscale*, 4:4301-4326, 2012.

[9] S. Sadat, A. Tan, Y.J. Chua and P. Reddy. Nanoscale thermometry using point contact thermocouples. Nano Letters, 10:2613-2617, 2010.

[10] S.K. Nezhadian, G. Rezazadeh and S.K. Arya. Mems tunneling micro thermometer based on tip deflection of bimetallic cantilever beam. *Sensors and Transducers*, 84:1660-1668, 2007.

[11] G. W. Walker, V. C. Sundar, C. M. Rudzinski, A. W. Wun, M. G. Bawendi and D. G. Nocera, Quantum-dot optical temperature probes, *Applied Physics Letters*, 83:3555–3557, 2003.

[12] D. Valerini, A. Creti, M. Lomascolo, L. Manna, R. Cingolani and M. Anni. Temperature dependence of the photoluminescence properties of colloidal CdSe/ZnS core/shell quantum dots embedded in a polystyrene matrix. *Physical Review B*, 71:235409, 2005.

[13] R.K.P. Benninger, Y. Koc, O. Hofmann, J. Requejo-Isidro, M.A.A. Nei, P.M.W. French and A.J. deMello. Quantitative 3D Mapping of Fluidic Temperatures within Microchannel Networks Using Fluorescence Lifetime Imaging. *Analytical Chemistry*, 78:2272-2278, 2006.

[14] S. Uchiyama, N. Kawai, A.P. de Silva and K. Iwai. Fluorescent Polymeric AND Logic Gate with Temperature and pH as Inputs. *Journal of the American Chemical Society*, 126:3032-3033, 2004.

[15] H. Kusuma, O.J. Sovers and T. Yoshioka. Line shift method for phosphor temperature measurements. *Japanese Journal of Applied Physics*, 15:2349-2358, 1976.

[16] Y. Shen, X. Wang, H. He, Y. Lin and C. Nan. Temperature sensing with fluorescence intensity ratio technique in epoxy-based nanocomposite filled with Er^{3+}-doped 7YSZ. *Composites Science and Technology*, 72:1008-1011.

[17] S.K. Singh, K. Kumar and S.B. Rai. Er^{3+}/Yb^{3+} codoped Gd_2O_3 nano-phosphor for optical thermometry. *Sensors and Actuators A*, 149:16-20, 2009.

[18] L. P. Goss, A. A. Smith and M. E. Post. Surface thermometry by laser-induced fluorescence. *Review of Scientific Instruments*, 60:3702-3706, 1989.

[19] N. Ishiwada, T. Ueda and T. Yokomori. Characteristics of rare earth (RE = Eu, Tb, Tm)-doped Y_2O_3 phosphors for thermometry. *Luminescence*, 26:381-389, 2010.

Chapter 2 - Synthesis of supported Y_2O_3:Ln NPs on α-Al_2O_3

2.1 Introduction

The aim of this work is to synthesize luminescent Ln-doped Y_2O_3 NPs (Ln = Eu^{3+}, Dy^{3+} or Er^{3+}/Yb^{3+}) on α-Al_2O_3 for temperature probing in catalytic environments. For this purpose, Y_2O_3 is chosen as host material for luminescent lanthanides because of its high thermal and chemical stability [1] in combination with a low phonon energy, resulting in efficient emission.[2] The material α-Al_2O_3 was utilized to support the Y_2O_3:Ln NPs. This material is widely used in catalysis since it exhibits excellent thermal and chemical stability.[3,4] Furthermore, due to its non-porosity the luminescent NPs remain on the surface of the support which makes the characterization easier and guarantees that the luminescence of the Y_2O_3:Ln NPs retains visible for the surroundings.

In this chapter, two methods are described to synthesize Y_2O_3:Ln NPs on α-Al_2O_3. Firstly, wet impregnation is exploited to synthesize NPs directly on α-Al_2O_3. The advantage of this method is that the synthesis is relatively easy.[4,5] Figure 2-1 shows a schematical illustration of this technique. RE metal nitrate precursors (*e.g.* $RE(NO_3)_3 \cdot x\ H_2O$ with RE = Y^{3+}, Eu^{3+}, Dy^{3+}, Er^{3+} and/or Yb^{3+}) are dissolved in water and added to α-Al_2O_3. The drying of the system results in the formation of a precursor-layer on the α-Al_2O_3, shown in the figure as a blue layer. Calcination at elevated temperatures converts the precursor-layer in the corresponding metal oxide phase, yielding Ln-doped Y_2O_3.

Secondly, the deposition of as-synthesized Y_2O_3:Ln NPs on α-Al_2O_3 is investigated, the procedure is schematically depicted in Figure 2-2. To gain a high control over the formation of the Y_2O_3:Ln NPs, the NPs are separately synthesized by homogeneous precipitation.[6,7] Afterwards, the as-synthesized NPs are dispersed in ethanol and deposited on α-Al_2O_3 by drying and physisorption.

Since the thermal and mechanical stability of the complexes are of high importance, adsorption and thermal experiments are carried out. The mechanical stability is examined by shaking Y_2O_3:Ln NPs / α-Al_2O_3 complexes in ethanol for specific times. The thermal stability was investigated by heating a sample at 600 °C for 12 h.

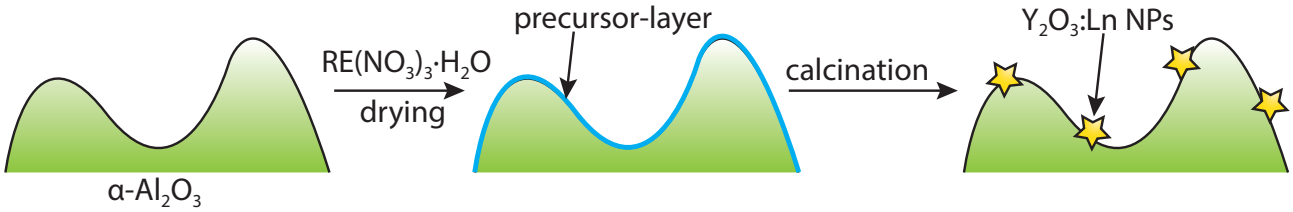

Figure 2-1: Schematic representation of wet impregnation of α-Al_2O_3 with Y_2O_3:Ln NPs. A precursor layer is formed after the drying of the nitrate solution and is converted to an Y_2O_3:Ln phase after calcination at elevated temperatures.

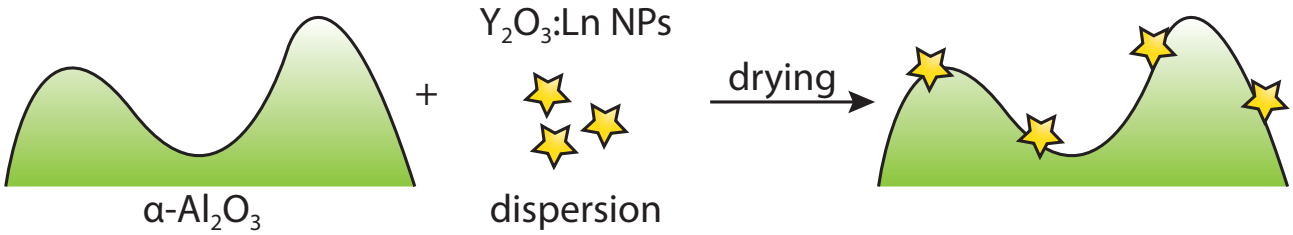

Figure 2-2: Schematic representation of the deposition of Y_2O_3:Ln NPs on α-Al_2O_3. A dispersion of Y_2O_3:Ln NPs is added to α-Al_2O_3 and dried, yielding Y_2O_3:Ln NPs / α-Al_2O_3 complexes.

2.2 Theory

1. Catalysis

Most conversions in the chemical industry are accelerated by catalysts which speed up the reaction. The majority of these conversions (80 %) make use of a heterogeneous catalyst where the catalyst itself is located in a different phase than the reactants.[3] In contrast to homogeneous catalysis, where the catalyst is dissolved in the liquid phase, heterogeneous catalysis takes place on the interface between a solid-liquid or a solid-gas interface.

Heterogeneous catalysts can be divided into two types: bulk and supported catalysts. Bulk catalysts are solely made of the active material, which contains the catalytic active sites, and are mainly used when the material is cheap. However, it is impossible to produce a bulk catalyst when the active component is expensive and/or made of rare elements. To overcome the use of these precious elements metal or metal oxide nanoparticles (NPs) are made to generate an excessive surface to volume ratio. The catalytic activity is consequently enhanced since the actual conversion takes place at the surface of these NPs.[8] Furthermore, the size decrease leads to an increase in the number of surface defects which are catalytically more active by the presence of different local electronic structures.[9] However, due to the large specific surface area the active NPs are less thermodynamically stable than their bulk counterparts. The size decrease leads to an excess of surface energy which is solved by the stabilization of the NPs on support materials.

A typical heterogeneous catalyst constitutes of an active phase, a support material and occasionally a promoter. The active phase comprises NPs containing the active sites where the actual conversion from reactant(s) to product(s) takes place. These NPs are generally between 1 and 100 nm in size and comprise 1 to 25 wt% of the total catalyst mass.[3] To deposit large numbers of catalytic NPs, porous support marials with high-surface-to-volume ratios materials are used. Relatively inexpensive and chemically stable materials such as carbon, SiO_2, TiO_2 and γ-Al_2O_3 are used as support.[3,4]

2. α-Al_2O_3 as support material for luminescent Y_2O_3:Ln NPs

In this thesis, we make use of α-Al_2O_3 as support material for luminescent Y_2O_3:Ln NPs since it exhibits various advantageous properties. Currently, α-Al_2O_3 is a widely used support material for catalyst NPs. It is used in applications such as methane reforming or epoxidation of propylene by utilizing nickel and gold NPs, respectively.[10,11] α-Al_2O_3 is chemically inert and exhibits high chemical and thermal stability. It withstands temperatures up to 1100 °C and is almost indissoluble in strong acids.[4] Although most phases of Al_2O_3, *e.g.* γ- and χ-Al_2O_3, are porous, the α-Al_2O_3 phase has been chosen to support luminescent Y_2O_3:Ln NPs since the material is non-porous. The deposited NPs will remain on the surface of the material. This makes characterization easier and guarantees that luminescence of Y_2O_3:Ln NPs is observable.

3. Wet impregnation of α-Al_2O_3

Wet impregnation is a widely used method for the synthesis of catalytic NPs (*e.g.* Ag, Co, Cu and, Fe_2O_3 NPs) on support materials such as α-Al_2O_3, CeO_2, TiO_2 or SiO_2.[11-15] This technique is relatively easy and environmentally friendly since low amounts of waste are generated.[5] In the first step of the synthesis, metal precursors, *e.g.* metal sulfates, carbonates, chlorides, nitrates or acetates, are dissolved in a solvent. In most cases, water is used because of the high solubility of many precursors. The formation of premature deposits of the metal precursor in bulk solution is prevented by lowering the dissolved amount of metal precursor below the (super)saturation concentration. After the addition of the solution to the support material the sample is dried to eliminate the solvent, resulting in the formation of a precursor-layer. Finally, the precursor-layer is at elevated temperatures converted into the corresponding metal oxide.

4. Synthesis of Y_2O_3:Ln NPs by homogeneous precipitation

Here, we make use of homogeneous precipitation, a liquid synthesis method which is extensively used for the synthesis of Y_2O_3 NPs. The method is capable of controlling the size and shape of the NPs to a high level.[6,7] Since the rare earth metals exhibit similar physical and chemical properties (see also the theory section of Chapter 3), the Y_2O_3 lattice can easily be doped with luminescent ions such as Eu^{3+}, Dy^{3+}, Er^{3+} and Yb^{3+} during the precipitation reaction.

The products of a decomposed organic compound, in this case urea, precipitate with metal cations in an aqueous solution. This results in the formation of precipitated nuclei above a critical point of super-saturation. Thereupon, the concentration of anions in solution is lowered while further generated anions are solely consumed by growth of the nuclei. The drop in anion concentration results in a well-defined separation of nucleation and growth which generates monodisperse NPs.

Urea (NH_2COHN_2) decomposes above 80 ºC in water into NH_4OH and H_2CO_3 (equation 1). The decomposed products NH_4OH and H_2CO_3 can react further to NH^{4+} and CO_3^{2-}, see equations 2, 3 and 4.

$$NH_2COHN_2 + 4\ H_2O \rightarrow 2\ NH_4OH + H_2CO_3 \qquad \text{Equation 2.1}$$

$$NH_4OH \longleftrightarrow NH_4^+ + OH^- \qquad \text{Equation 2.2}$$

$$H_2CO_3 \longleftrightarrow H^+ + HCO_3^- \qquad \text{Equation 2.3}$$

$$HCO_3^- \longleftrightarrow H^+ + CO_3^{2-} \qquad \text{Equation 2.4}$$

Yttrium, as well as other RE metal ions, precipitate with OH^-, CO_3^{2-} and 1.5 H_2O as:

$$Y^{3+} + OH^- + CO_3^{2-} + 1.5\ H_2O \rightarrow Y(OH)CO_3 \cdot 1.5\ H_2O \qquad \text{Equation 2.5}$$

The hydrous precipitate $Y(OH)CO_3 \cdot 1.5\ H_2O$ is converted into the anhydrous product $Y(OH)CO_3$ at a temperature of 200 ºC.[6] Finally, at temperatures above 640 ºC $Y(OH)CO_3$ is transformed into the corresponding oxide to yield the metal oxide product Y_2O_3.

2.3 Methods

1. Synthesis of Y_2O_3:$Eu_{0.05}$ NPs on α-Al_2O_3 by wet impregnation

The chemicals $Y(NO_3)_3 \cdot 6H_2O$ and $Eu(NO_3)_3 \cdot 6H_2O$ were purchased from Sigma-Aldrich. Extrudates of α-Al_2O_3 (BASF) were thoroughly grinded to obtain a white powder. All chemicals were used without further purification.

Supported co-doped Y_2O_3:$Eu_{0.05}$ NPs on α-Al_2O_3 flakes with different weight loadings (5, 10 and 20 wt.%) were prepared by the wet impregnation technique. The nitrate precursors $Y(NO_3)_3 \cdot 6H_2O$ and $Eu(NO_3)_3 \cdot 6H_2O$ were in the molar ratio 0.95/0.05 dissolved in water and added to α-Al_2O_3. The obtained slurry was dried under continuous stirring and heating at 85 °C. When the water was evaporated the samples were calcined in static air for 3 hours using a ramp of 5 °C/min.

2. Synthesis of Y_2O_3:Ln NPs by homogeneous precipitation

The chemicals $Y(NO_3)_3 \cdot 6H_2O$, $Eu(NO_3)_3 \cdot 6H_2O$, $Dy(NO_3)_3 \cdot 6H_2O$, $Er(NO_3)_3 \cdot 6H_2O$ and $Yb(NO_3)_3 \cdot 6H_2O$ (all 99.99% purity) were purchased from Sigma-Aldrich. Urea (99.5% purity) and ethanol (100% purity, containing traces of H_2O) were purchased from Strem Chemicals. All chemicals were used without further purification.

The preparation of the Y_2O_3:Ln NPs is based on the methods of Sohn and Fukushima.[6,7] In all experiments, 178.5 mL of purified water was added to a round-bottom flask and 240 µmol of urea was consequently dissolved while stirring vigorously. Then, a solution of 0.72 mmol RE in 1.5 mL water was added to the urea solution to yield a total RE^{3+} concentration of 0.004 M in 180 mL solution.

The solution was heated under stirring at 85 ºC while measuring the pH every 20 minutes. After a subsequent strong decline and slow rise of the pH, the heating was stopped and the solution cooled naturally down to room temperature. A representative pH versus time diagram is enclosed in Appendix 2.7.1. Afterwards, the solutions were centrifuged, washed three times with water and finally dispersed in 2 mL ethanol to prevent aggregation. The samples were dried overnight at 60 ºC and calcined in static air at 900 ºC for 3 hours using a ramp of 5 ºC/min.

3. Deposition of Y_2O_3:Ln NPs on α-Al_2O_3 by drying

Various masses of Y_2O_3:Ln NPs, made by homogenous precipitation, and α-Al_2O_3 (spherical powder of 20-50 micron, Alfa Aesar) were weighed for loadings of 0.1, 1, 5, 10 and 20 wt% to yield a total mass of 300 mg Y_2O_3:Ln NPs / α-Al_2O_3. The NPs were dispersed in ethanol by sonicating up to 60 min to obtain a white dispersion with a concentration of 5 mg NPs/mL EtOH. The liquid fraction of the dispersion was taken by a pipette, leaving eventual non-dispersible grains behind on the bottom of the flask. The dispersion was consequently added to α-Al_2O_3 and carefully shaked for one minute. Afterwards, the samples were dried overnight at 60 ºC.

4. Deposition of Y_2O_3:Ln NPs on α-Al_2O_3 by physisorption

Y_2O_3:Ln NPs, made by homogenous precipitation, were dispersed in ethanol by sonicating for 60 minutes to obtain a white dispersion with a concentration of 5 mg NPs/mL EtOH. α-Al_2O_3 (spherical powder of 20-50 µm, Alfa Aesar) was added to a filter (Whatman type 1001, pore size of 11 µm) and the dispersion was subsequently added, see also Figure 2-3. The system was rested for 5 minutes to let the NPs adsorb on the α-Al_2O_3. Finally, the excess of NPs was removed by washing the system by the addition of 5 mL in steps of 1 mL per minute and dried at 60 ºC overnight.

5. Adsorption and mechanical stability of Y_2O_3:Ln NPs on α-Al_2O_3

An as-synthesized sample of 5 wt% Y_2O_3:$Eu_{0.05}$ NPs / α-Al_2O_3, made by drying deposition, was divided in equal amounts of 50 mg and brought into separate Eppendorf tubes. 2 mL ethanol was added to each tube and placed on a roller shaker for various periods of time. Afterwards, the Y_2O_3:$Eu_{0.05}$ NPs / α-Al_2O_3 complexes were separated from the liquid phase by resting the tubes for 5 min to let

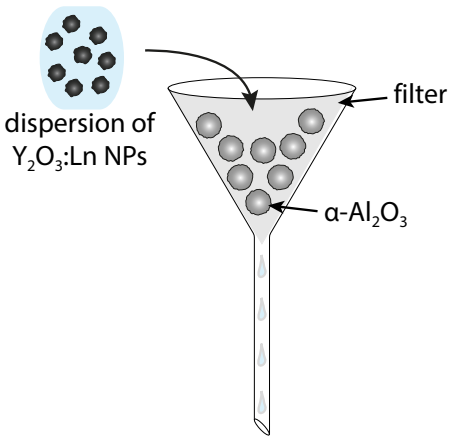

Figure 2-3: Schematic representation (not on scale) of the deposition of Y_2O_3:Ln NPs on α-Al_2O_3 by physisorptionin a funnel.

the microspheres sedimentate to the bottom of the flask. The dispersion, containing the desorbed NPs, was removed and analyzed with ICP-OES. The $Y_2O_3:Eu_{0.05}$ NPs / α-Al_2O_3 complexes were dried at 60 ºC and characterized with SEM. The thermal stability of an as-synthesized sample was examined by heating the sample for 12 h at 600 ºC in static air using a ramp of 5 ºC/min.

6. Characterization techniques

XRD diffractograms were recorded on a PW 1729 Philips diffractometer utilizing Cu Kα radiation between 2θ = 15 and 80º. TEM images were taken with a Tecnai 10 Philips microscope at 15 keV using a BSE detector. SEM images were made on a FEI XL30S FEG operating at 15 kV. Concentrations were measured with ICP on a Perkin-Elmer Optima 8300 Optical Emission Spectrometer.

2.4 Results and discussion

1. Synthesis of Y_2O_3:$Eu_{0.05}$ NPs on α-Al_2O_3 by wet impregnation

In this study, Y_2O_3:Ln NPs were synthesized on the support α-Al_2O_3 by wet impregnation. Samples were made with loadings of 5, 10 and 20 wt% Y_2O_3:$Eu_{0.05}$ and calcined at 750 ºC for 10 h. XRD diffractograms were recorded to investigate the formed phase on α-Al_2O_3. The results are shown in Figure 2-4 (a) with reference diffractograms of Y_2O_3 (red), aluminium (blue) and α-Al_2O_3. As can be seen, similar diffraction peaks are found for consecutive loadings and confirm the synthesis of an Y_2O_3 phase next to α-Al_2O_3. The peaks corresponding to the Y_2O_3 phase become more present with increasing Y_2O_3 loading, this observation is in agreement with the presence of a higher amount of Y_2O_3 at higher weight loadings.

Furthermore, the average crystallite size of the Y_2O_3 phase was determined using the Scherrer equation by exploiting the most intense peaks of the Y_2O_3 phase. Figure 2-4 (b) shows the calculated crystallite size versus the Y_2O_3 loading. By varying the Y_2O_3 loading from 5 to 20 wt% the crystallite size increases from 10.0 nm to 11.4 nm. Although an increase in crystallite size is observed, the change is insignificant to be attributed to the change of Y_2O_3 loading.

To investigate the Y_2O_3:$Eu_{0.05}$ phase on the surface of α-Al_2O_3, TEM images were obtained which are shown in Figure 2-5. The typical smooth micrometer-sized flakes of α-Al_2O_3 are visible with NPs and layers of Y_2O_3:$Eu_{0.05}$ at various spots. However, the majority of α-Al_2O_3 did not contain any Y_2O_3:$Eu_{0.05}$ NPs or layers. Low loadings, viz. 5 and 10 wt%, result in the formation of single NPs although layers up to 45 nm thick are found as well. The loading of 20 wt% generates thicker layers with thicknesses up to 55 nm. Temperature probing with high accuracy requires well-defined NPs which cover the α-Al_2O_3 homogeneously. Since these requirements are not met, these complexes are not suitable for temperature probing.

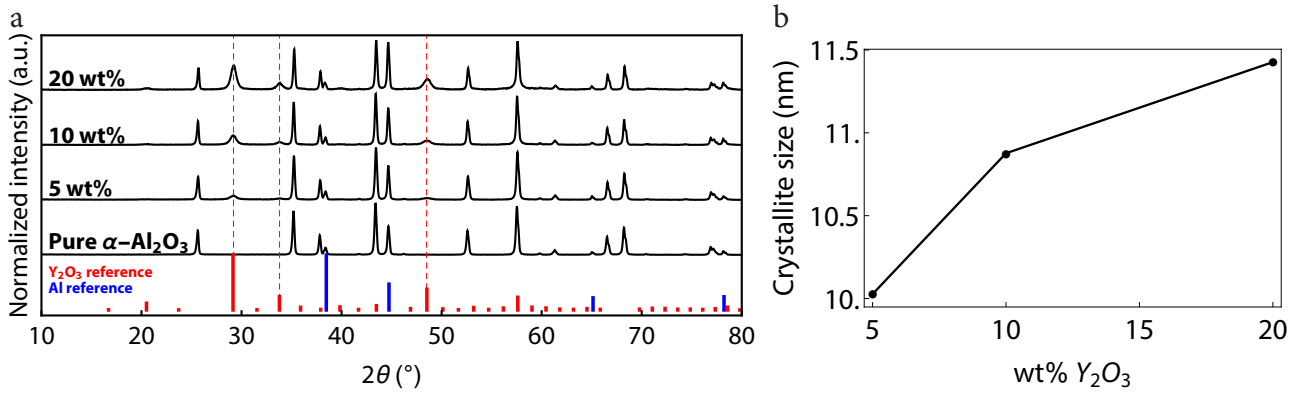

Figure 2-4: (a) XRD diffractograms of 5, 10 and 20 wt% Y_2O_3:$Eu_{0.05}$ / α-Al_2O_3 calcined at 750 °C for 10 h with reference diffractograms of α-Al_2O_3, Y_2O_3 (red) and aluminium (blue). Dashed red lines indicate the used peaks for the calculation of the crystallite size of Y_2O_3. The aluminium phase is present by the usage of an aluminium sample holder. (b) Calculated crystallite sizes of the Y_2O_3 phase XRD diffractograms using the Scherrer equation using the peaks at 2θ = 29.1, 33.8 and 48.5°.

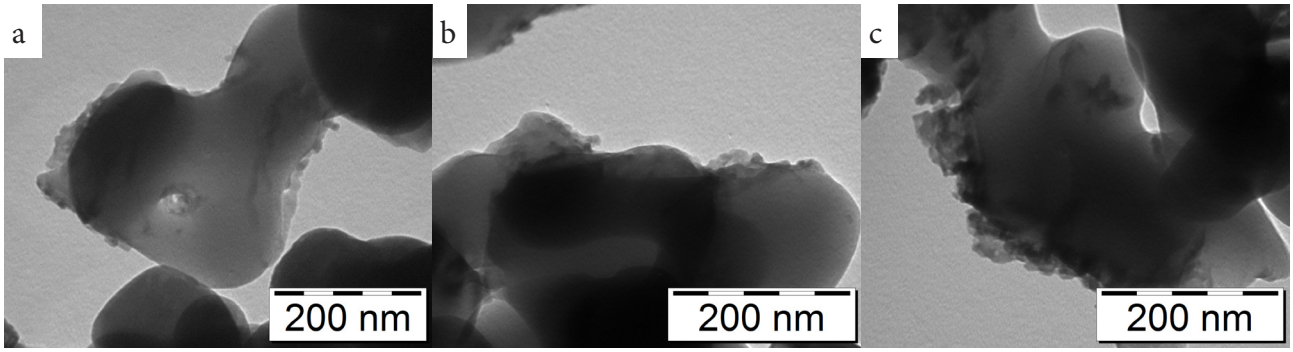

Figure 2-5: TEM images of Y_2O_3 / α-Al_2O_3 flakes calcined at 750 °C for 10 h with loadings of (a) 5, (b) 10 and (c) 20 wt% Y_2O_3:Ln.

2. Influence of the calcination temperature on the synthesis of Y_2O_3:$Eu_{0.05}$ NPs on α-Al_2O_3

The calcination step was further investigated to study the influence of the calcination temperature on the formation of the Y_2O_3 phase. Calcination of the sample took place at 750 ºC, followed by calcination at 850, 1000 and 1100 ºC, each cycle had a duration of 10 h. Figure 2-6 shows the XRD diffractograms with reference diffractograms of pure α-Al_2O_3, Y_2O_3 (red bars) and $Y_4Al_2O_7$ (YAM, yttrium aluminium monoclinic, blue bars). In the XRD diffractograms of the samples calcined at 750 and 850 ºC the characteristic peaks of the Y_2O_3 on α-Al_2O_3 phases are visible with Y_2O_3 crystallite sizes of 10.1 and 10.2 nm, respectively. However, samples calcined at 1000 and 1100 ºC show the presence of YAM instead of Y_2O_3. This implicates that calcination at 1000 ºC is high enough to mobilize Y^{3+} and Al^{3+} ions what results in the incorporation of Y^{3+} atoms into α-Al_2O_3, yielding $Y_4Al_2O_7$. Figure 2-7 shows a TEM image of 20 wt% Y_2O_3/α-Al_2O_3 that has been calcined at 1100 ºC. As can be seen, the YAM phase on α-Al_2O_3 exhibits a smooth surface and is not well-defined. The formation of YAM on α-Al_2O_3 is unfavourable because temperature probing requires single luminescent Y_2O_3 NPs.

From above results it can be concluded that wet impregnation is unsuitable for the synthesis of supported Y_2O_3:Ln NPs on α-Al_2O_3. Wet impregnation of α-Al_2O_3 favours the formation of an Y_2O_3 layer on different spots above the formation of single Y_2O_3:$Eu_{0.05}$ NPs. Increasing the weight loading results in the formation of Y_2O_3 layers whereas at higher calcination temperatures Y atoms are incorporated into the α-Al_2O_3 phase.

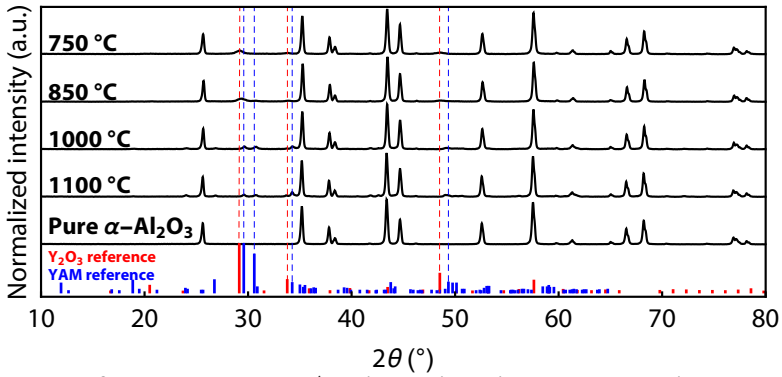

Figure 2-6: XRD diffractograms of 5 wt% Y_2O_3:$Eu_{0.05}$ / α-Al_2O_3 calcined at 750, 850 and 1000 °C for 10 h with reference diffractograms of α-Al_2O_3, Y_2O_3 (red) and aluminium (blue). Dashed red lines indicate the used peaks for crystallite size calculation of Y_2O_3 for the samples calcined at 750 and 850 °C.

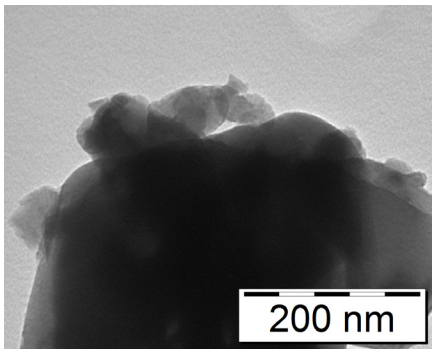

Figure 2-7: TEM image of 20 wt% Y_2O_3 / α-Al_2O_3 flakes calcined at 1100 °C for 10 h.

3. Synthesis of Y_2O_3:Ln NPs by homogeneous precipitation

Y_2O_3:Ln (Ln = Eu^{3+}, Dy^{3+} or Er^{3+}/Yb^{3+}) NPs were synthesized by homogeneous precipitation with urea. To determine the size and shape of the as-synthesized NPs, TEM images were taken. In Figure 2-8 representative images are shown of precursor and calcined Y_2O_3:$Eu_{0.05}$ NPs, respectively.

Precursor NPs, shown in Figura 2-8 (a), appear as smooth and spherical particles and are occasionally interconnected. In Figure 2-8 (b) it can be seen that after calcination NPs with an uniform spherical shape and morphology with a rough surface are obtained. Furthermore, contrast differences are observed within calcined NPs which arise by the presence of crystallite domains. It has been proposed that the increase in surface roughness by the calcination step is the result of the evaporation of chemically bonded H_2O and CO_2. A pressure build-up inside the particles due to the evaporation of gases leads to cracks within the NP and increased surface roughness.[6]

The size and polydispersity of the NPs before and after calcination was calculated from TEM-images for all Y_2O_3:Ln samples, the results are shown in Table 2-1. As can be seen, the diameter of the precursor NPs varies between 70 and 285 nm with polydispersities ranging from 7.2 nm to 33.2 nm. It is unclear what the reason is for these size variations.

It was found that the particle size decreases upon calcination. Calcination of the precursor NPs yields NPs between 50 nm and 245 nm in diameter with polydispersities from 8.5 nm up to 33.8 nm. Sohn *et al.* related the densities of precursor and calcined NPs to the decrease of NP volume during calcination. The densities of $Y(OH)CO_3 \cdot 1.5\ H_2O$ and Y_2O_3 are ca. 3.9 and 5.0 g/cm^3 which corresponds to a size decrease of 23 % in diameter for spherical particles.[6] From above measurements, size decreases between 11 and 24 % have been found. The majority of the samples, except for Y_2O_3:$Eu_{0.05}$ (sample BS050), Y_2O_3:$Er_{0.01}Yb_{0.01}$ and Y_2O_3:$Dy_{0.0085}$ NPs, show size decreases between 20 and 24% which are in the same of the order of magnitude as expected. However, Y_2O_3:$Er_{0.01}Yb_{0.01}$ and Y_2O_3:$Dy_{0.0085}$ exhibit smaller size decreases of 14 and 16 %, respectively. The smaller change in particle size decrease upon calcination is attributed to the large size of as-synthesized NPs.

To confirm the crystallite phase of the as-synthesized NPs, XRD diffractograms were recorded. Figure 2-9 shows the results of Y_2O_3:$Eu_{0.05}$, Y_2O_3:$Dy_{0.0085}$,Y_2O_3:$Er_{0.02}Yb_{0.05}$ samples with reference patterns of pure Y_2O_3 (red) and aluminium (blue). The Y_2O_3 phase is clearly present and is not altered by the presence of dopants. The absence of additional diffraction peaks from dopants can be due to

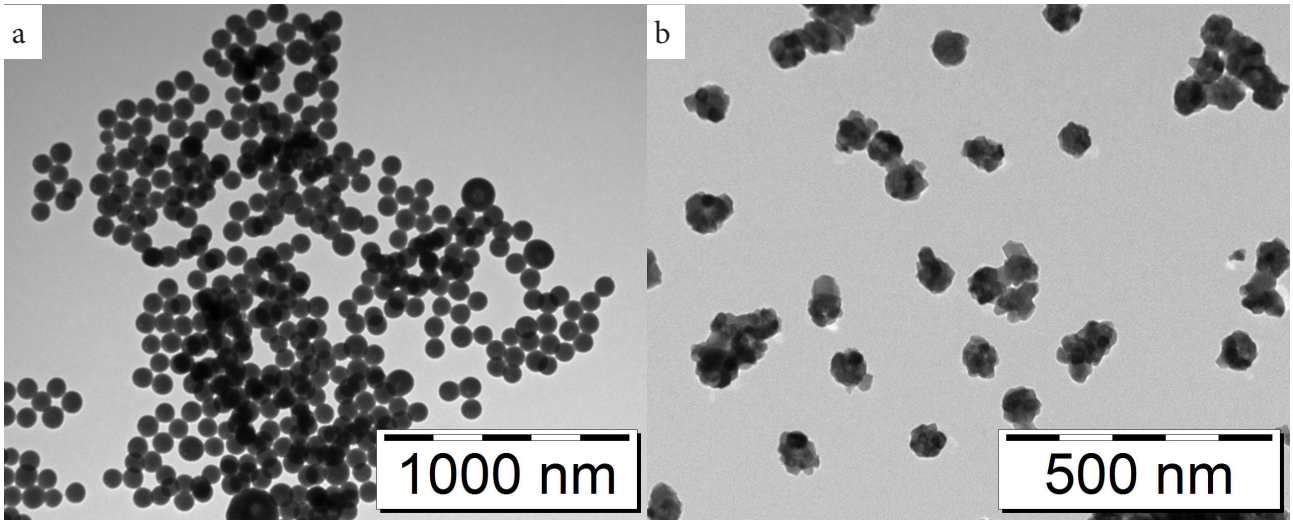

Figure 2-8: Representative TEM images of uncalcined (a) and calcined (b) Y_2O_3:$Eu_{0.05}$ NPs.

two different reasons. As mentioned in the theory section of Chapter 3, rare earth metals have almost similar atomic radii which subsequently results in almost equal diffraction peaks. Furthermore, the dopant concentrations are too low to have a significant effect on the diffraction patterns.

As can be seen, all samples show shifted diffraction peaks in comparison to reference patterns. This shift is caused by the usage of partially filled sample holders since the synthesized amount of NPs is not sufficient to fill the holders completely. Due to the partially filled holders the reflection of x-rays is detected at slightly different angles. Nevertheless, the shift will not affect the calculations of the average crystallite sizes since the peak widths are unaffected. The average crystallite sizes by exploiting the Scherrer equation were found to be 17.5, 18.0 and 20.6 nm for the Y_2O_3:$Eu_{0.05}$, Y_2O_3:$Dy_{0.0085}$ and Y_2O_3:$Er_{0.02}Yb_{0.05}$ samples, respectively.

To confirm the incorporation of the Eu^{3+}, Dy^{3+}, Er^{3+} and Yb^{3+} ions in the Y_2O_3 lattice, ICP measurements were carried out. Table 2-2 shows the results with the expected concentrations between brackets. As can be seen, the majority of measured concentrations are in agreement with the expected values. However, the Yb^{3+} concentration in the Y_2O_3:$Er_{0.02}Yb_{0.05}$ sample is lower than expected. A possible explanation for this is that the synthesis of this sample is incorrectly carried out, *e.g.* unsufficient $Yb(NO)_3$ precursor solution was added to the reaction mixture.

Table 2-1: Size and polydispersity of Y_2O_3:Ln NPs (Ln = Eu^{3+}, Dy^{3+} or Er^{3+}/Yb^{3+}) determined from TEM-images.

		Precursor NPs		Calcined NPs		
Sample	Contents	Size (nm)	Polydispersity (nm)	Size (nm)	Polydispersity (nm)	Size decrease (%)
BS050	Y_2O_3:$Eu_{0.05}$	80.4	8.9	71.4	9.9	11
BS059	Y_2O_3:$Eu_{0.05}$	71.8	7.2	54.3	10.4	24
BS057	Y_2O_3:$Er_{0.02}$	92.9	9.6	70.9	6.1	24
BS058	Y_2O_3:$Er_{0.02}Yb_{0.05}$	105.4	11.0	82.1	9.9	22
BS061	Y_2O_3:$Er_{0.01}Yb_{0.01}$	282.4	33.2	242.4	33.8	14
BS062	Y_2O_3:$Er_{0.001}Yb_{0.01}$	114.0	9.5	91.2	8.5	20
BS056	Y_2O_3:$Dy_{0.0085}$	162.0	22.9	135.3	18.4	16

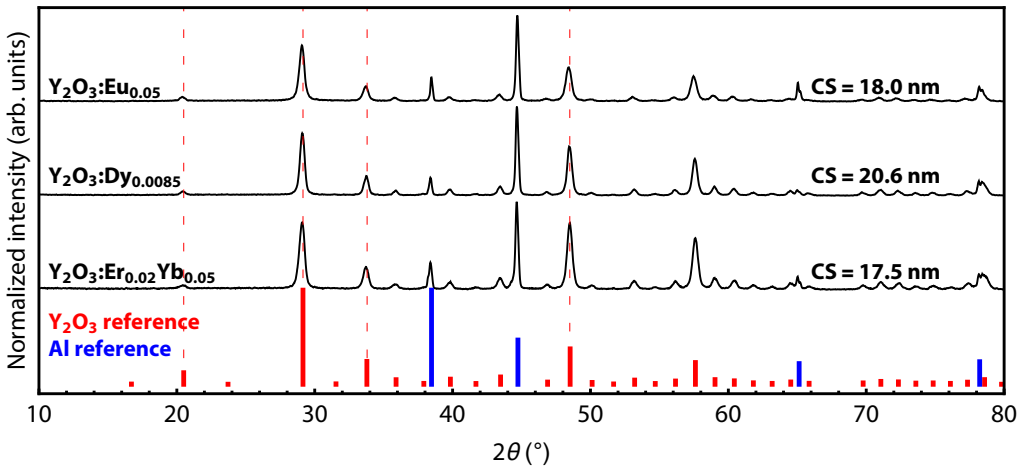

Figure 2-9: XRD diffractograms of Y_2O_3:$Eu_{0.05}$, Y_2O_3:$Dy_{0.05}Ce_{0.0085}$ and Y_2O_3:$Er_{0.02}Yb_{0.05}$ with reference patterns of Y_2O_3 (red) and aluminium (blue). The samples were measured in an aluminium sample holder, generating the characteristic peaks of the aluminium phase. Crystallite sizes (CS) were calculated from the peaks at 2θ = 20.5, 29.2, 33.8 and 48.5 °.

Table 2-2: Concentrations of dopants from ICP measurements of the Y_2O_3:Ln NPs (Ln = Eu^{3+}, Dy^{3+} or Er^{3+}/Yb^{3+}), values between brackets refer to the theoretical concentrations.

Sample	Contents	Eu (%)	Er (%)	Yb (%)	Dy (%)
BS050	$Y_2O_3:Eu_{0.05}$	4.8 (5.0)			
BS057	$Y_2O_3:Er_{0.02}$		2.0 (2.0)		
BS058	$Y_2O_3:Er_{0.02}Yb_{0.05}$		2.1 (2.0)	3.5 (5.0)	
BS061	$Y_2O_3:Er_{0.01}Yb_{0.01}$		1.0 (1.0)	0.7 (1.0)	
BS062	$Y_2O_3:Er_{0.001}Yb_{0.01}$		0.1 (0.1)	0.7 (1.0)	
BS056	$Y_2O_3:Dy_{0.0085}$				0.9 (0.85)

4. Influence of calcination temperature on crystallite size and morphology

It is of high importance to obtain a crystallite size as large as possible since the luminescence can be quenched by defects in the lattice, *e.g.* line defects or ion vacancies. Calcination at higher temperatures yields a less disordered crystal structure with an enhanced crystallite size.[16,17]

To study the influence of the calcination temperature on the crystallite size and morphology of Y_2O_3:Ln NPs, an uncalcined sample of $Y_2O_3:Eu_{0.05}$ was calcined successively at 700, 800, 900, 1000 and 1100 ºC. Figure 2-9 (a) and (b) show the XRD diffractograms and the average crystallite sizes calculated with the Scherrer equation, respectively. As can be seen, an amorphous phase is obtained of the uncalcined sample directly after synthesis. Calcination of the as-synthesized sample yields the characteristic Y_2O_3 phase. Moreover, it can be seen in Figure 2-10 (b) that with increasing the calcination temperature from 700 to 1100 ºC, the crystallite size increases from 15 to 27 nm which is in line with our expectations.

Size and shape of the NPs was confirmed with TEM after each calcination step. Figure 2-11 and Figure 2-12 show the TEM images and size measurements of the NPs, respectively. The image of the uncalcined NPs, see Figure 2-11 (a), shows monodisperse spherical particles with an average diameter of 72.6 nm. The images of calcination at 700 and 800 ºC are shown in Figure 2-11 (b) and (c). As can be seen, the spherical morphology is preserved although the size is decreased to 57.2 and 57.5 nm, respectively. Furthermore, the rough surface and contrast differences from the NPs arises by diffraction of the electron beam of the crystal domains. Successive calcination at 900, 1000 and 1100 ºC, see Figure 2-11 (d)-(f), increases the average particle size and yields cubical-shaped NPs. Moreover, the NPs are sintered to form larger particles up to 104.4 nm in diameter.

The results show that the calcination temperature is a critical parameter for the shape and crystallite size of the Y_2O_3:Ln NPs. At relatively low calcination temperatures, *viz.* 700 and 800 ºC, spherical particles are synthesized with crystallite sizes of 15.1 and 17.1 nm, respectively. Calcination at 900, 1000 and 1100 results in interconnected NPs of cubical size and shape which makes the particle unsuitable. From this it is clear that the optimal calcination temperature is 800 ºC.

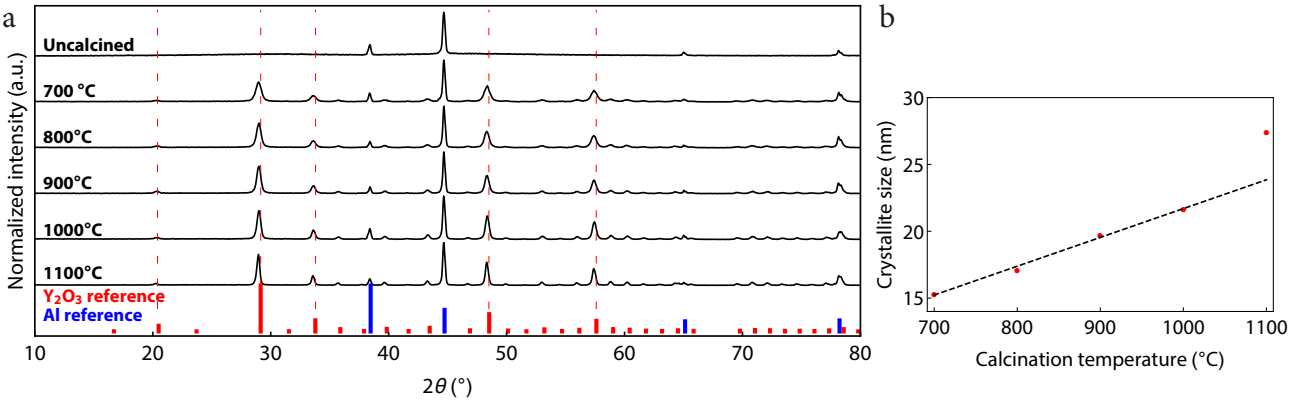

Figure 2-10: (a): XRD diffractograms of Y_2O_3:$Eu_{0.05}$ NPs calcined at 700, 800, 900, 1000 and 1100 °C and reference diffractograms of Y_2O_3 (red) and aluminium (blue). The samples were measured in an aluminium sample holder, generating the characteristic peaks of the aluminium phase. (b): Calculated average crystallite size versus calcination temperature using the Scherrer equation and the peaks at 2θ = 20.5, 29.2, 33.8 and 48.5°.

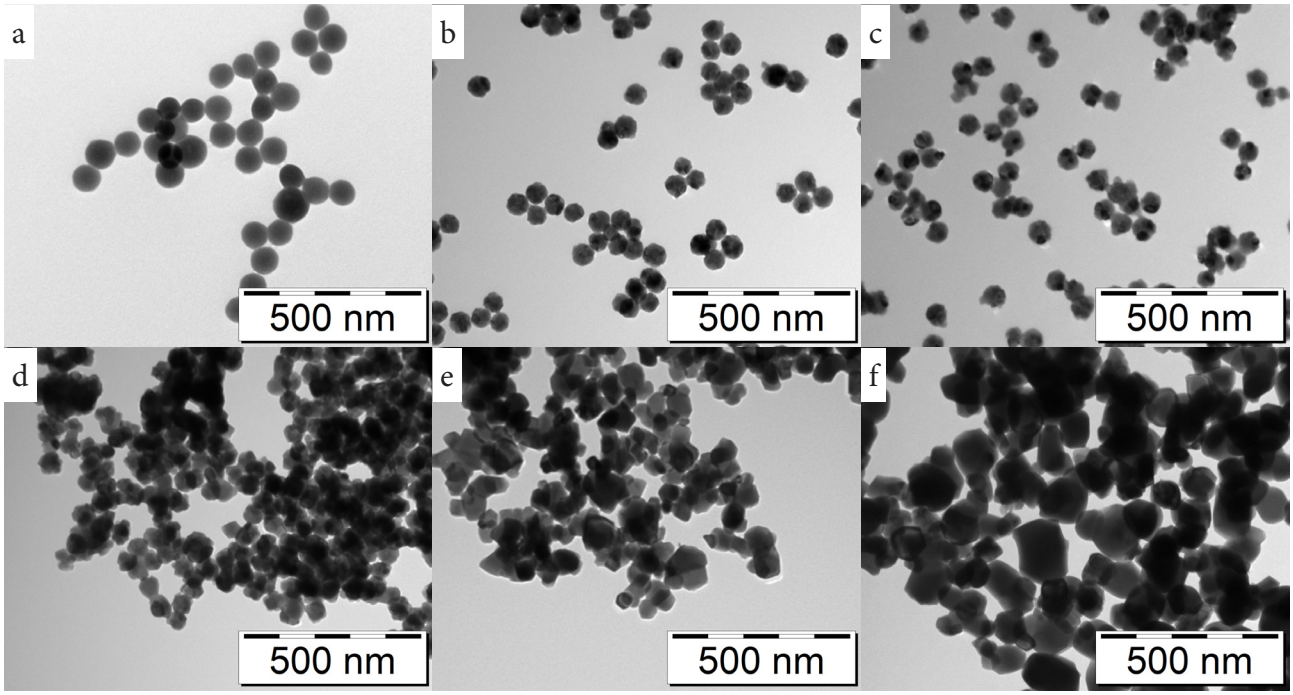

Figure 2-11: TEM images of uncalcined Y_2O_3:$Eu_{0.05}$ NPs (a) and calcined NPs at 700 (b), 800 (c), 900 (d), 1000 (e) and 1100 °C (f).

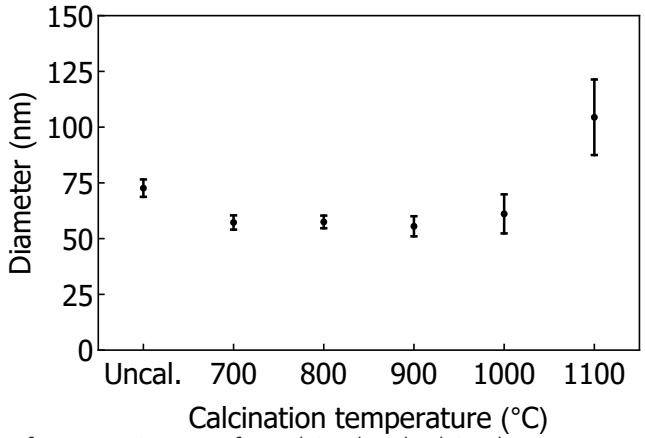

Figure 2-12: Size measurements from TEM images of uncalcined and calcined Y_2O_3:$Eu_{0.05}$ NPs at 700, 800, 900, 1000 and 1100 °C, error bars indicate the standard deviation.

5. Deposition of Y_2O_3:Ln NPs on α-Al_2O_3 by drying

The goal of this chapter is to explore the preparation of Y_2O_3:Ln NPs / α-Al_2O_3 complexes for temperature probing in catalytic environments. Since it highly preferred to utilize the complexes afterwards with catalytic active NPs on the surface of α-Al_2O_3, several requirements have to be fulfilled. The luminescent NPs have to be homogeneously distributed over the surface and exhibit sufficient luminescence for successful temperature probing. Moreover, unoccupied space is required for the deposition of catalytic NPs. Therefore, a balance between the amount of luminescent and catalytic NPs has to be found. To investigate these requirements several weight loadings of Y_2O_3:$Eu_{0.05}$ NPs on α-Al_2O_3 were prepared.

First, the morphology and microstructure of unmodified α-Al_2O_3 was examined with SEM. Figure 2-13 shows SEM images of a representative α-Al_2O_3 particle (a) and a zoom-in of the surface (b). As can be seen, the α-Al_2O_3 has a spherical morphology and is generally between 20 and 75 µm in size and contain protrusions up to approximately 1 µm. Moreover, the typical smooth structures of α-Al_2O_3 are clearly present on the surface.

Several samples of Y_2O_3:$Eu_{0.05}$ NPs on α-Al_2O_3 were prepared to investigate the influence of the weight loading on the surface density of NPs. The NPs were deposited on α-Al_2O_3 by drying Y_2O_3:$Eu_{0.05}$ NPs dispersions, yielding weight loadings of 0.1, 1.0, 5.0 and 10.0 wt%. The theoretical and experimental weight loadings are equivalent since the entire dispersion is deposited on α-Al_2O_3. After deposition, the resulting products were characterized with XRD and SEM to examine the morphology and microstructure of the samples.

Figure 2-14 shows the XRD diffractograms of Y_2O_3:$Eu_{0.05}$ NPs, α-Al_2O_3 and Y_2O_3:$Eu_{0.05}$ NPs/α-Al_2O_3 complexes. As can be seen, the diffractogram of Y_2O_3:$Eu_{0.05}$ NPs / α-Al_2O_3 exhibits both diffraction peaks of the Y_2O_3 and α-Al_2O_3 phase, confirming the deposition of the NPs on the support material. Furthermore, the crystallite size of the NPs is preserved, indicating that the NPs are not affected by the deposition.

The SEM images of the complexes with weight loadings of 0.1, 1.0, 5. and 10 wt%, shown in Figure 2-15, show white NPs on the grey α-Al_2O_3 spheres. The contrast arises by the difference in atomic mass of the strong back-scattering yttrium and weak back-scattering aluminium atoms. This difference can be visualized in SEM analysis when using a back-scattering detector. As can be seen in the images, the density of NPs on the surface increases with increasing weight loading which is in agreement with our expectations. The surface is homogeneously covered at loadings of 0.1 and 1.0 wt% whereas at 5.0 wt% NP-clusters up to 500 nm in size are observed. A loading of 10 wt% results in a partly filled surface although other places are covered with µm-size clustered NPs.

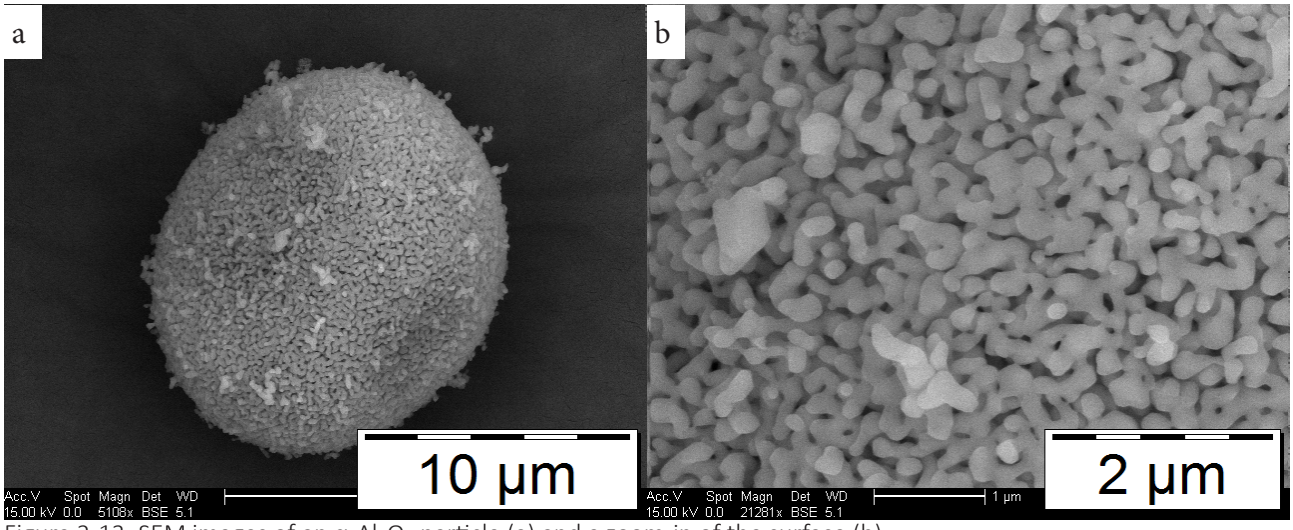

Figure 2-13: SEM images of an α-Al_2O_3 particle (a) and a zoom-in of the surface (b).

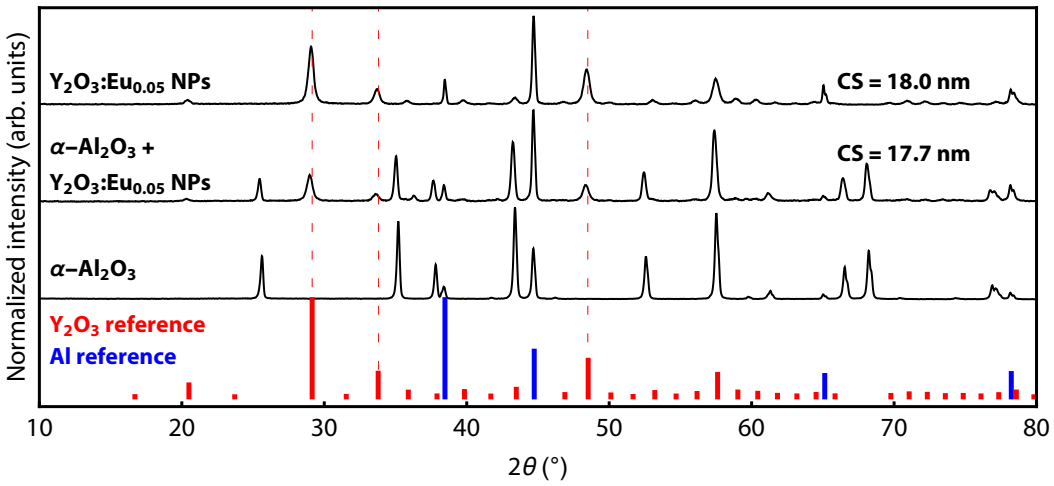

Figure 2-14: XRD diffractograms of Y_2O_3:$Eu_{0.05}$ NPs and deposited Y_2O_3:$Eu_{0.05}$ NPs on α-Al_2O_3. The crystallite sizes (CS) were calculated from the peaks at 2θ = 20.5, 29.2, 33.8 and 48.5°. Reference diffractograms are shown of α-Al_2O_3, Y_2O_3 (red bars) and aluminium (blue bars).

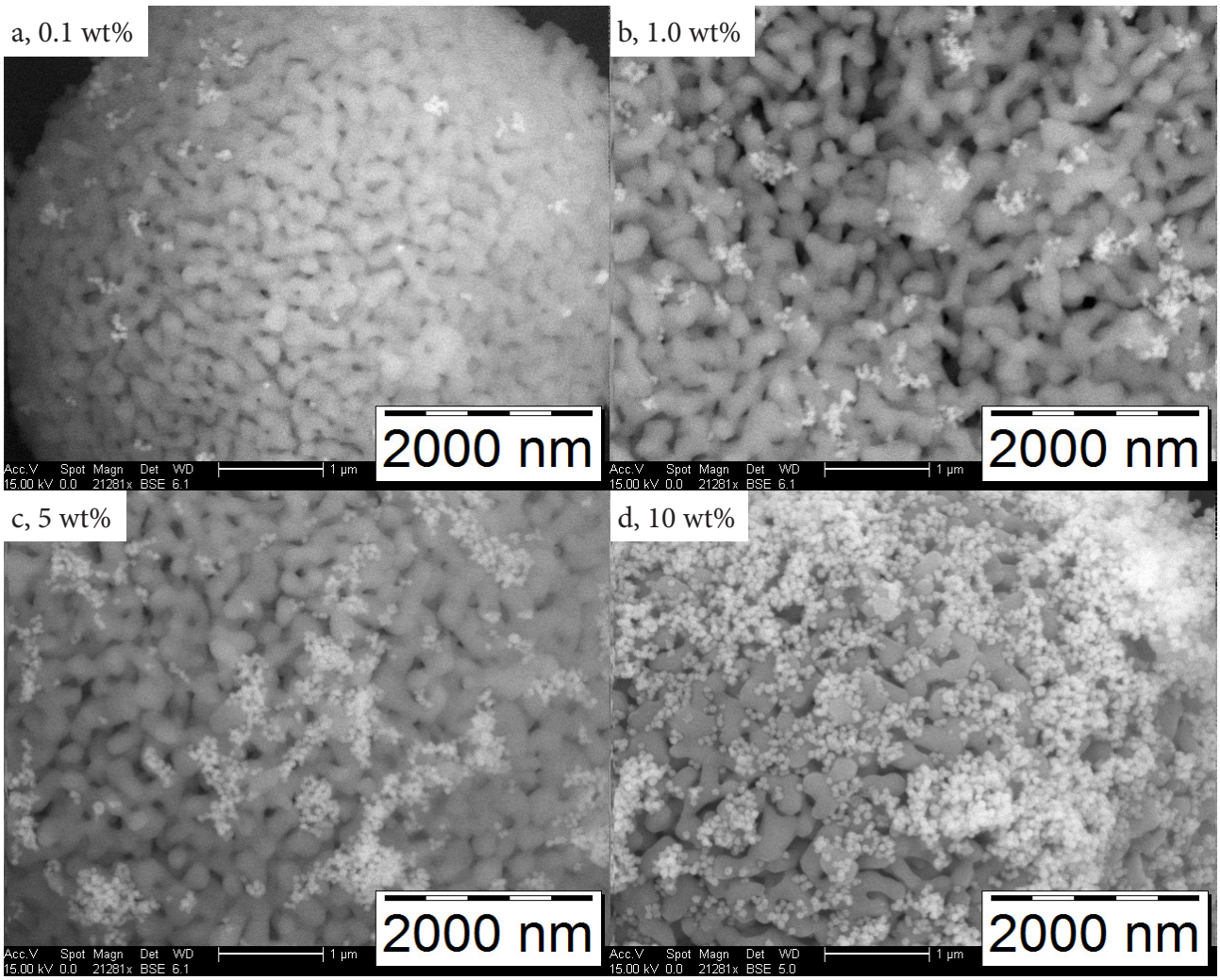

Figure 2-15: SEM images of the surface of α-Al_2O_3 with different loadings of Y_2O_3:$Eu_{0.05}$ NPs made by drying deposition: 0.1 wt% (a), 1.0 wt% (b), 5.0 wt% (c) and 10.0 wt% (d).

The clustering of NPs that is observed at all loadings could be attributed to various reasons. Firstly, as can be seen on the TEM images of calcined samples (Figure 2-8 (b)), the NPs are directly after preparation occasionally clustered. Secondly, when nearly all ethanol is evaporated, most Y_2O_3:Ln NPs will remain in the dispersion, resulting in specific spots where the remaining ethanol will evaporate, leaving clusters of NPs behind. Lastly, since the Y_2O_3:Ln NPs are not stabilized by ligands, the NPs could be clustered by *e.g.* electrostatic interactions.

From above results it can be concluded that the optimal loading is 5 wt% Y_2O_3:$Eu_{0.05}$ on the α-Al_2O_3. Weight loadings of 0.1 and 1.0 wt% will result in weak luminescence whereas the formation of large NP-clusters at 10 wt% has to be avoided. The weight loading of 5 wt% results in the formation of a homogeneous surface coverage while the luminescence is preserved. Furthermore, sufficient space on the surface is available for the deposition of catalytic NPs next to the luminescent Y_2O_3:Ln NPs.

6. Deposition of Y_2O_3:Ln NPs on α-Al_2O_3 by physisorption

To investigate the physisorption of Y_2O_3:Ln NPs on α-Al_2O_3, Y_2O_3:$Eu_{0.05}$ NPs were deposited on α-Al_2O_3 by physisorption deposition. The benefit of this method is that exclusively adsorbed NPs are deposited on α-Al_2O_3 whereas the excess is washed away. From this experiment, it can be determined if the Y_2O_3:Ln NPs exhibit affinity for the surface of α-Al_2O_3. This affinity could not be deduced from the previous method, deposition by drying, since the total dispersion is dried on α-Al_2O_3.

Therefore, a certain amount of Y_2O_3:$Eu_{0.05}$ NPs was dispersed in ethanol for a loading of 5 wt%. The dispersion was added to the α-Al_2O_3, which was placed in a funnel with a filter. Directly after addition, the filter partly absorbed the dispersion and characteristic red luminescence was observed from the Y_2O_3:$Eu_{0.05}$ NPs under excitation of an UV-lamp (λ_{exc} = 254 nm). Based on this observation, it can already be expected that not all NPs are deposited on the α-Al_2O_3.

To examine the surface of α-Al_2O_3 after deposition, SEM images were taken. The images are shown in Figure 2-16 for an α-Al_2O_3 particle and a zoom-in of the surface. As can be seen on the images, the surface is homogeneously covered with Y_2O_3:$Eu_{0.05}$ NPs. Moreover, the density of NPs is lower and the NPs are more homogeneously distributed over the surfaces in comparison to the sample of 5 wt% Y_2O_3:$Eu_{0.05}$ / α-Al_2O_3 prepared with drying deposition (Figure 2-17 (c)). This observation also confirms our hypothesis that not all Y_2O_3:$Eu_{0.05}$ are adsorbed by the α-Al_2O_3.

Although the actual weight loading could not be determined from the SEM images, a rough estimate of the weight loading can be made by comparing the images with known weight loadings prepared by drying deposition.

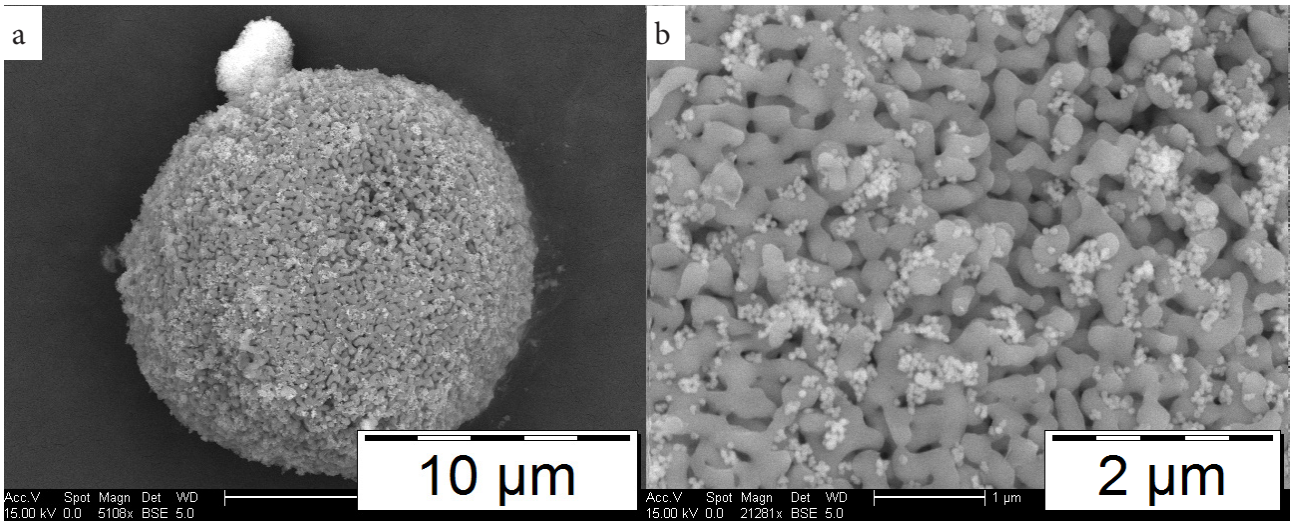

Figure 2-16: SEM images of α-Al_2O_3 after the deposition of Y_2O_3:$Eu_{0.05}$ particles by physisorption. An image of an α-Al_2O_3 paricle (a) and a zoom-in of the surface (b).

7. Thermal stability of Y_2O_3:Ln NPs on α-Al_2O_3

The majority of catalytic reactions in the chemical industry occur at temperatures up to 600 ºC. This makes it of high importance that the Y_2O_3:Ln NPs on α-Al_2O_3 are thermally stable. To examine this aspect, a sample of 10 wt% Y_2O_3:$Eu_{0.05}$ NPs / α-Al_2O_3 complexes was thermally treated for 12 h at 600 ºC. It is expected that the complexes are not altered by the thermal treatment since both Y_2O_3 and α-Al_2O_3 exhibit high thermal stability.

To examine the morphology of the sample before and after the thermal treatment, SEM images of the sample were taken. The results are shown in Figure 2-17 for the sample before (a)-(b) and after the thermal treatment (c)-(d). The NPs are clearly visible on the surface of the α-Al_2O_3 before and after the treatment. As discussed in the previous section, a loading of 10 wt% results in large clusters of NPs on the surface of α-Al_2O_3 which is visible on these SEM images as well. Nevertheless, no major differences such as sintering or changes in particle morphology are observed after the heating treatment.

To investigate the influence of the thermal treatment on the crystal phases, XRD diffractograms were recorded. The results are shown in Figure 2-18. As can be seen, the peaks of the Y_2O_3 and Al_2O_3 phases are obviously present and are not affected by the thermal treatment. Furthermore, the calculated crystallite size of the Y_2O_3 phase was determined before and after and have an identical size of 17.7 nm, confirming the thermal stability of the complexes.

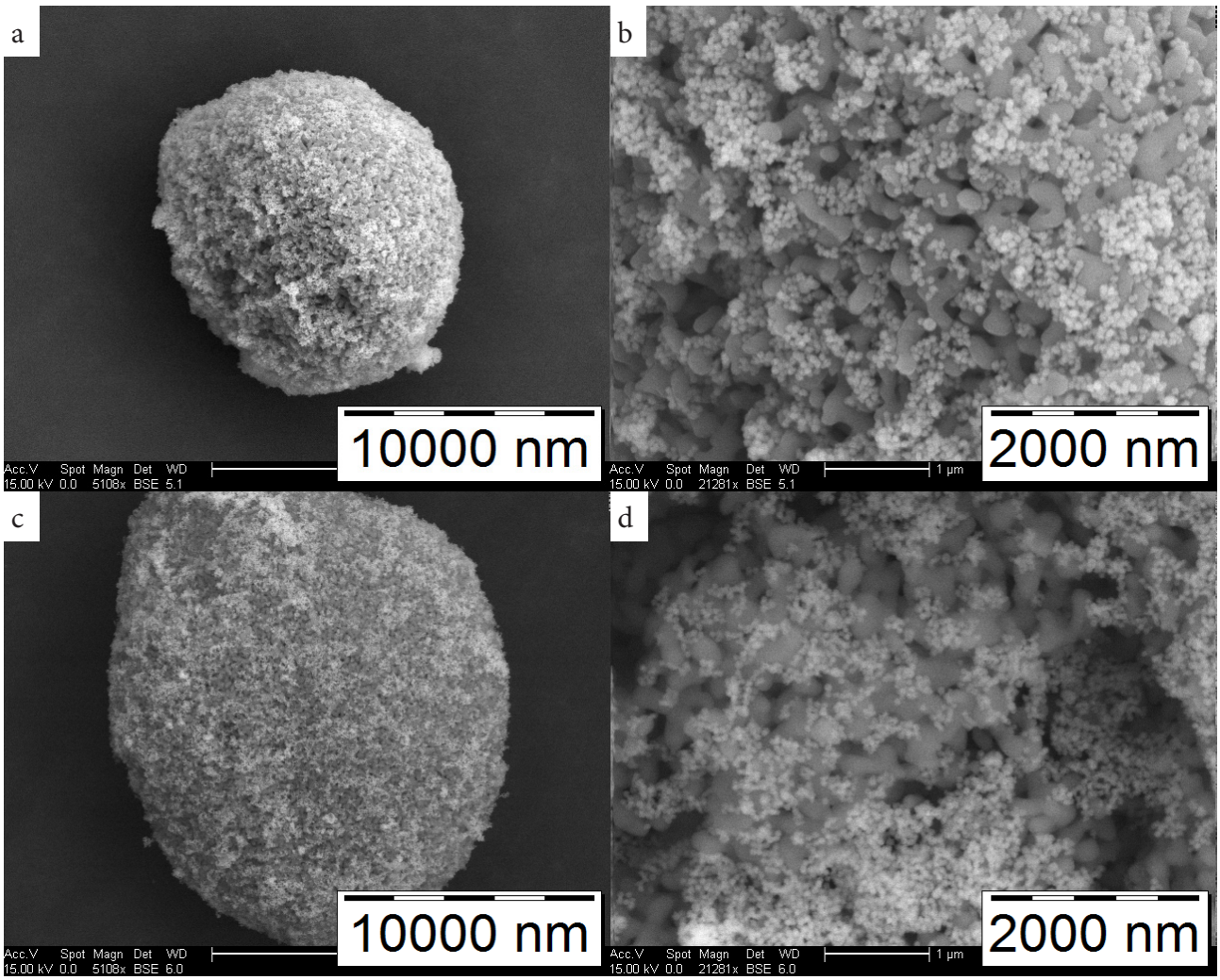

Figure 2-17: SEM images of 10 wt% Y_2O_3:Ln NPs / α-Al_2O_3 before (a & b) and after (c & d) a heating treatment for 12h at 600 °C.

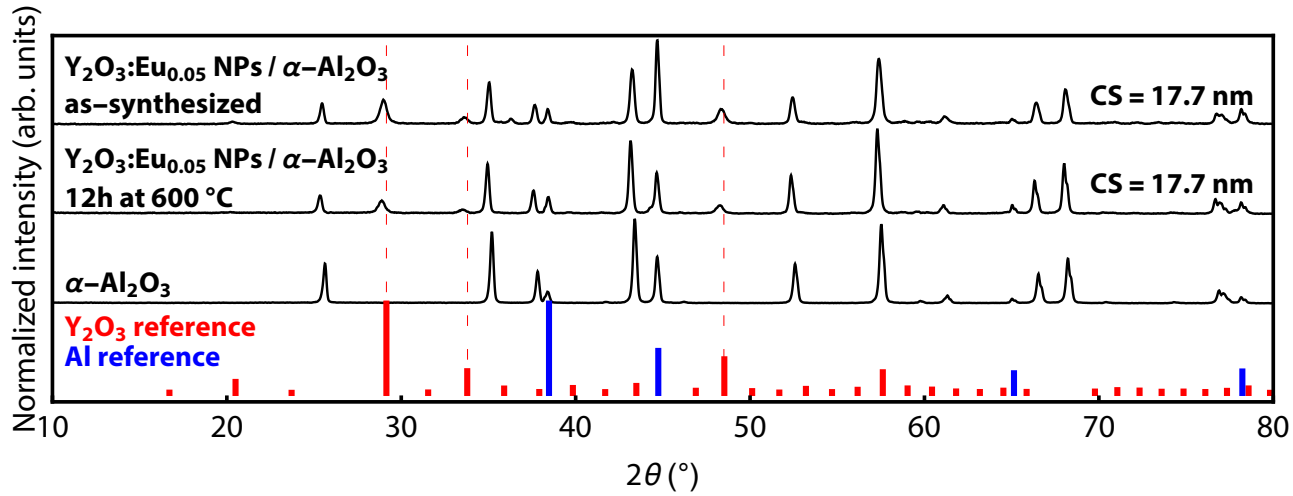

Figure 2-18: XRD diffractograms of as-synthesized and thermal treated samples of 10 wt% Y_2O_3:$Eu_{0.05}$ / α-Al_2O_3. The thermal treated sample was heated for 12 h at 600 °C. Reference diffractograms are shown of α-Al_2O_3, Y_2O_3 (red bars) and aluminium (blue bars). The crystallite sizes (CS) were calculated from the peaks at 2θ = 20.5, 29.2, 33.8 and 48.5°.

8. Mechanical stability of Y_2O_3:Ln NPs on α-Al_2O_3

When embedded in a reactor, it is of high importance that the Y_2O_3:Ln NPs exhibit a strong affinity for the surface of α-Al_2O_3. Otherwise, the deposited Y_2O_3:Ln NPs will be released into the mobile phase. This leads to the contamination of the liquid or gas phase and decreases the luminescence which consequently enhances the difficulty of temperature probing.

To study the mechanical stability of Y_2O_3:Ln NPs on α-Al_2O_3 in a representative solvent, an as-synthesized sample of 5 wt% Y_2O_3:$Eu_{0.05}$ / α-Al_2O_3 was added to ethanol and placed on a roller shaker up to 24 h. Afterwards, the samples were examined with SEM to study the microstructure and morphology. Figure 2-19 shows images of as-synthesized and samples exposured to ethanol for 1 min and 24 h. Images of samples shaked for 0.5, 1, 4 and 8 h are enclosed in Appendix 2.7.3. As can be seen on the images, the Y_2O_3:$Eu_{0.05}$ NPs are present on the surface of the α-Al_2O_3 after the exposure of ethanol. No clustering or changes in particle morphology are observed with increasing exposure time. Furthermore, the density of NPs remains constant which indicates that the particles remain adhered on the surface.

ICP measurements of the ethanol phase indicated the absence of NPs in ethanol. Only in the sample that was exposed for 24 hours an yttrium concentration in the detection limit of the machine was measured, indicating an insignificant desorption of NPs leaching to the liquid phase. From this, it can be concluded that the Y_2O_3:Ln NPs remain adhered on α-Al_2O_3 during exposure of ethanol.

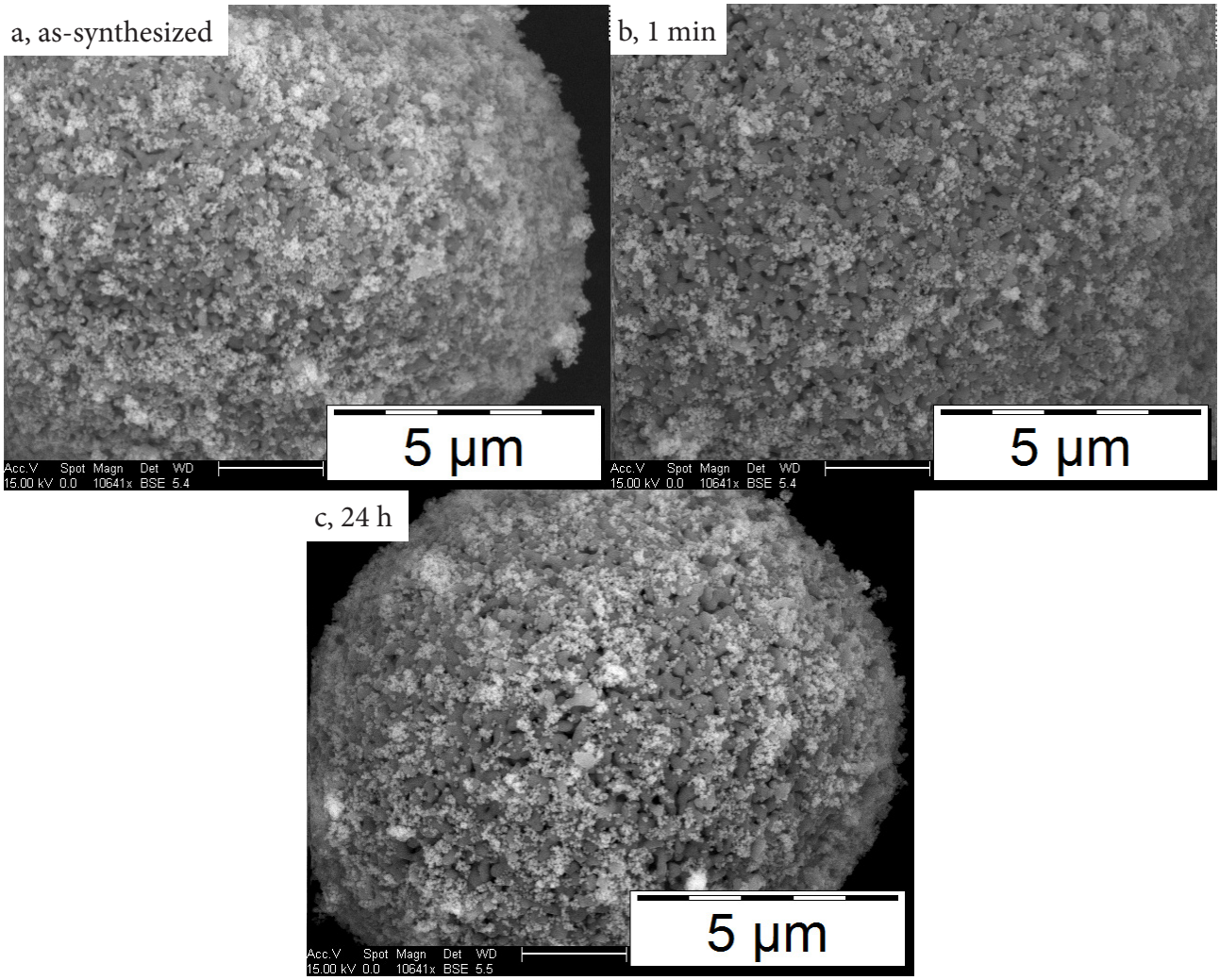

Figure 2-19: SEM images of 5 wt% Y_2O_3:$Eu_{0.05}$ NPs / α-Al_2O_3 after shaking the complexes in EtOH for different periods of time. Images of as-synthesized complexes (a) and samples shaked for 1 min (b) and 24 h (c).

2.5 Conclusion

In this chapter the synthesis of Y_2O_3:Ln (Ln = Eu^{3+}, Dy^{3+} and Er^{3+}/Yb^{3+}) NPs / α-Al_2O_3 complexes was discussed. Wet impregnation, the direct synthesis of Y_2O_3:Ln on α-Al_2O_3, has shown to be unsuitable for the preparation of well-defined NPs since layers were formed at selective spots. Further investigation of the calcination step up to 1100 ºC did result in the unfavourable formation of $Y_4Al_2O_7$. Therefore, another approach was taken to gain a high control over the synthesis by separating the preparation of Y_2O_3:Ln NPs and deposition on α-Al_2O_3. It was found that Y_2O_3:Ln NPs between 50 and 250 nm in size were successfully synthesized. Afterwards, the Y_2O_3:Ln NPs were deposited on α-Al_2O_3 by drying and physisorption. The NPs were succesfully deposited on the surface and a loading of 5 wt% was found to be the optimal density. Furthermore, shaking and thermal experiments showed that the NPs were mechanically and thermally stable up to 600 ºC.

2.6 References

[1] W. M. Yen, S. Shionoya and H. Yamamoto, Phosphor Handbook. *CRC Press*, 2006.

[2] D. Matsuura. Red, green, and blue upconversion luminescence of trivalent-rare-earth ion-doped Y_2O_3 nanocrystals. *Applied Physics Letters 81*, 24:4256-4528.

[3] K.P. de Jong. Synthesis of solid catalysts. *Wiley-VCH*, 2009.

[4] J.R.H. Ross. Heterogeneous Catalysis, Fundamentals and Applications. Elsevier, 2012.

[5] P. Munnik, P.E. de Jongh and K.P. de Jong. Recent developments in the synthesis of supported catalysts. *Chemical Reviews*, 115:6687-6718, 2015.

[6] S. Sohn, Y. Kwon, Y. Kim and D. Kim. Synthesis and characterization of near-monodisperse yttria particles by homogeneous precipitation method. *Powder Technology*, 142:136-153, 2004.

[7] S. Fukushima, T. Furukawa, H. Niioka, M. Ichimiya, T. Sannomiya, J. Miyake, M. Ashida, T. Araki and M. Hashimoto. Synthesis of Y_2O_3 nanophosphors by homogeneous precipitation method using excessive urea for cathodoluminescence and upconversion luminescence bioimaging. *Optical Materials Express 6*, 3:831-843, 2016.

[8] J.M. Campelo, D. Luna, R. Luque, J. M. Marinas and A.A. Romero, Sustainable preparation of supported metal nanoparticles and their applications in catalysis. *ChemSusChem*, 2:18-45, 2009.

[9] W. Chen, H. Wang and R.A. Bartynski. Catalysis by materials with well-defined structures: Nanofaceted metal surfaces: structures, reactivity and applications. *Elsevier*, 2015.

[10] F. Pompeo, N.N. Nichio, M.M.V.M. Souza, D.V. Cesar, O.A. Ferretti and M. Schman. Study of Ni and Pt catalysts supported on α-Al_2O_3 and ZrO_2 applied in methane reforming with CO_2. *Applied Catalysis A*, 316:175-183, 2007.

[11] W. Yao, Y. Guo, X. Liu, Y. Guo, Y. Wang, Y. Wang, Z. Zhang and G. Lu. Epoxidation of propylene by molecular oxygen over the Ag-Y_2O_3-K_2O/α-Al_2O_3 catalyst. *Catalysis Letters*, 119:185-190, 2007.

[12] D.R. Sahoo, S. Vajpai, S. Patel and K.K. Pant. Kinetic modeling of steam reforming of ethanol for the production of hydrogen over Co/Al_2O_3 catalyst. *Chemical Engineering Journal*, 125:139-147, 2007.

[13] M. Fröba, R. Köhn and G. Bouffaud, Fe_2O_3 nanoparticles within mesoporous MCM-48 silica: *In situ* formation and characterization. *Chemical Materials*, 11:2858-2865, 1999.

[14] L.S. Yoong, F.K. Chong and B.K. Dutta. Development of copper-doped TiO_2 photocatalyst for hydrogen production under visible light. *Energy*, 34:1652-1661, 2009.

[15] T. Caputo, L. Lisi, R. Pirone, G. Russo. On the role of redox properties of CuO/CeO_2 catalysts in the preferential oxidation of CO in H_2-rich gases. *Applied Catalysis A: General*, 348:42-53, 2008.

[16] H. Guo, N. Dong, M. Yin, W. Zhang, L. Lou and S. Xia. Visible upconversion in rare earth ion-doped Gd_2O_3 nanocrystals. *Journal of Physical Chemistry B*, 108:19205-19209, 2004.

[17] C. de Mayrinck, D. P. Santos, S.J.L. Ribero, M.A. Schiavon and J.L. Ferrari. Reassessment of the potential application of Eu^{3+}-doped Y_2O_3 photoluminescent material in ceramic powder form. *Ceramics International*, 40:15965-15971, 2014.

2.7 Appendix

1. pH and temperature during the synthesis of Y_2O_3:$Eu_{0.05}$ NPs by homogeneous precipitation

Temperature and pH were monitored during precipitation to follow the process of NP formation, shown in Figure 2-19. A steep pH decrease is observed during the first 20 minutes by the generation of H^+ ions due to the decomposition of urea. The precipitation starts by the formation of nuclei what is observed by the change from a colorless to a white solution, indicated in the Figure by the dashed black line. The increase of pH due to the decomposition of the excess of urea indicates the finishing of the synthesis.

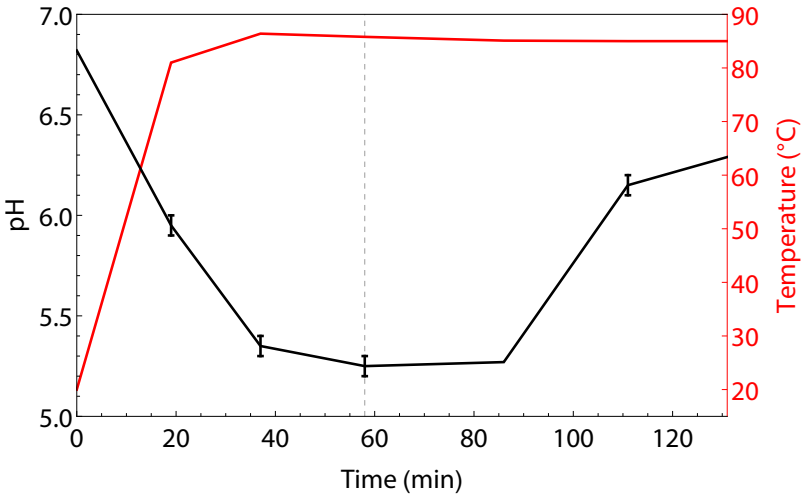

Figure 2-20: Temperature and pH during the synthesis of Y_2O_3:$Eu_{0.05}$ NPs. Error bars indicate the boundaries of pH measurements whereas the dashed black line indicate the first moment a white precipitate in the solution was visible to the naked eye.

2. Grains of Y_2O_3:$Eu_{0.05}$ NPs

A small fraction of calcined Y_2O_3:$Eu_{0.05}$ NPs could not be dispersed in EtOH and was left on the bottom of the flask. The grains were dried and characterized with SEM to study the morphology, see Figure 2-21. As can be seen, grains with dimensions up to 250 µm in size have been formed. The zoom-in shows the surface of such a grain, showing that the grain is consitutes of small particles.

Later on, it was found out that the final washing step of the precursor NPs is critical for the formation of these µm-sized grains. Incomplete redispersion, leaving a gel-like structure behind on the bottom of the drying tube, results in the formation of these particles. Full redispersation of the as-synthesized NPs resulted in an absence of these µm-sized NP grains.

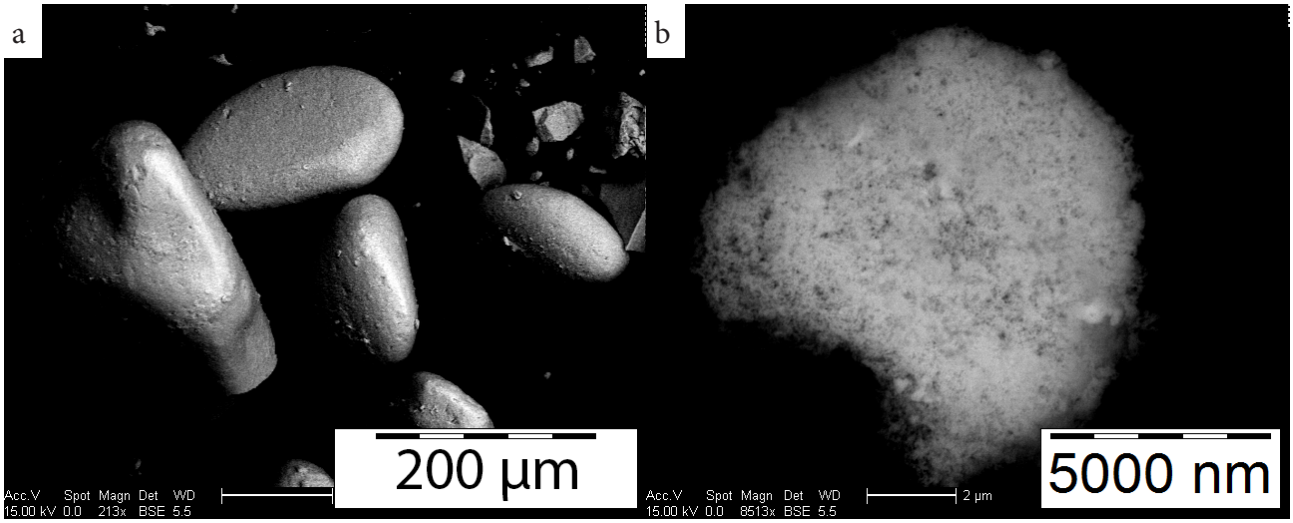

Figure 2-21: SEM images of undispersable Y_2O_3:Ln particles after drying (a), a zoom-in of the surface (b).

3. Mechanical stability of Y_2O_3:$Eu_{0.05}$ NPs on α-Al_2O_3

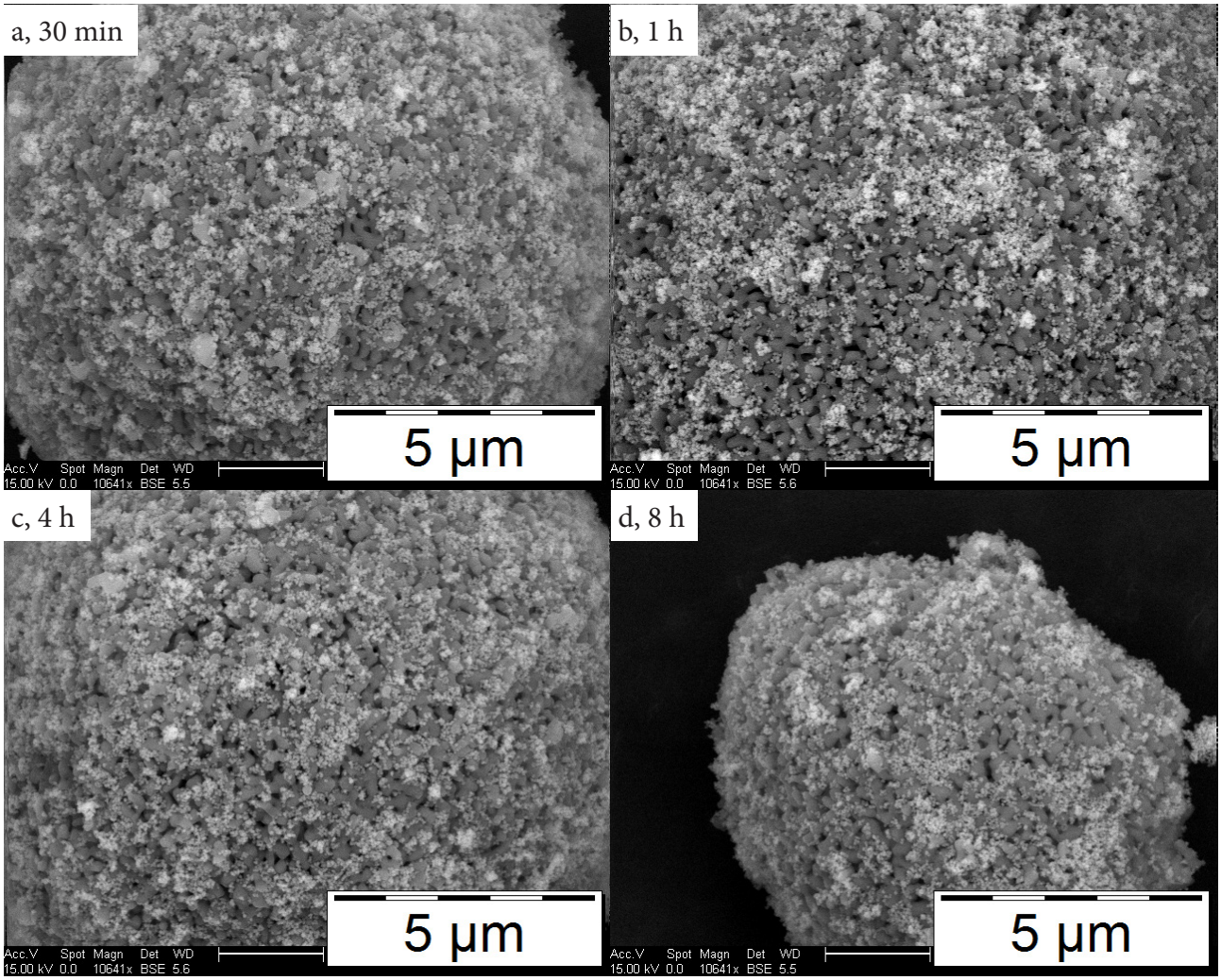

Figure 2-22: SEM images of 5 wt% Y_2O_3:$Eu_{0.05}$ NPs / α-Al_2O_3 after shaking the complexes in EtOH for 30 min (a), 1 h (b), 4 h (c) and 8 h (d).

Chapter 3 - Temperature dependent luminescence of Y_2O_3:Ln NPs on α-Al_2O_3

3.1 Introduction

The main aim of this work is to develop luminescent temperature probes for catalytic environments by exploiting temperature dependent emission from Y_2O_3:Ln NPs on α-Al_2O_3. In the previous chapter, the synthesis procedures of the complexes were discussed. The direct synthesis of NPs on α-Al_2O_3 by wet impregnation was found to be unsuitable since layers of Y_2O_3:Ln were formed instead of well-defined NPs. Therefore, another approach was taken by separating the synthesis and deposition of Y_2O_3:Ln NPs on α-Al_2O_3. The NPs were succesfully synthesized by homogeneous precipitation and afterwards deposited on α-Al_2O_3. Furthermore, thermal and adsorption stability experiments confirmed the stability of the complexes.

In this chapter, the luminescence of the Eu^{3+}, Dy^{3+}, and Er^{3+}/Yb^{3+}-doped Y_2O_3:Ln NPs on α-Al_2O_3 complexes is investigated. The complexes are examined by excitation and emission spectra. Furthermore, temperature dependent emission spectra between room temperature and 600 °C are recorded to investigate the luminescence up to high temperatures. To examine the reproducibility and accuracy of the temperature probes, thermal cycling experiments are performed.

3.2 Theory

Lanthanides

The lanthanides comprise the series of fifteen chemical elements with atomic numbers ranging from 57 up to 71, located at the bottom of the periodic table. Lanthanides are occassionaly entiteld as rare earth elements, or simply rare earths (RE). However, RE is not the correct definition since it also includes the elements yttrium (Y) and scandium (Sc), with $Z = 21$ and $Z = 39$, respectively.[cotton]

The lanthanide series starts with lanthanum (La) which has an electron configuration of [Xe] $5d^1$ $6s^2$ since the 5d orbital is lower in energy than a 4f orbital. However, further addition of protons result in the filling of 4f-orbitals as the 4f orbitals become rapidly more stable by contraction to the nucleus. This contraction is visualized in Figure 3-1 where the probabilities for observing 4f, 5d and 6s electrons are plotted versus the distance to the nucleus. As can be seen, the 4f orbitals are principally located near the nucleus whereas the 5d and 6s orbitals are spreaded out over larger volume.

Therefore, cerium (Ce) and praseodymium (Pr) have electron configurations of [Xe] $4f^1$ $5d^1$ $6s^2$ and [Xe] $4f^3$ $6s^2$, respectively. The filling of the f orbitals continues after praseodymium from neodymium up to europium (Eu) with configurations of [Xe] $4f^n$ $6s^2$ ($n = 4 - 7$), see also Table 3-1. Since a half-filled f orbital is lower in energy than that of a 5d orbital, the electron configuration of gadolinium (Gd) is [Xe] $4f^7$ $5d^1$ $6s^2$. After gadolinium, the pattern is continued from terbium (Tb) up to ytterbium (Yb), with [Xe] $4f^n$ $6s^2$ (n = 9 - 14). The series is completed by lutetium (Lu) where the last electron is placed in the 5d orbital, generating the [Xe] $4f^{14}$ $5d^1$ $6s^2$ configuration.

The common oxidation state of lanthanides is the trivalent oxidation state (Ln^{3+}), resulting in electron configurations of [Xe] $4f^n$, with n varying from $n = 0$ for lanthanum up to $n = 14$ for lutetium. An important characteristic of lanthanides is the complete shielding of the 4f orbitals by the fully filled 5s and 5p valence orbitals. The shielding is the principal reason for the chemical and spectroscopic properties, such as similar atomic and ionic radii, enthalpies of formation and ionization energies.[blasse] This in contrast to the d-block transition metals, where the d orbitals are not shielded by outerlying orbitals and the spectroscopic and magnetic properties are strongly affected by the surroundings.

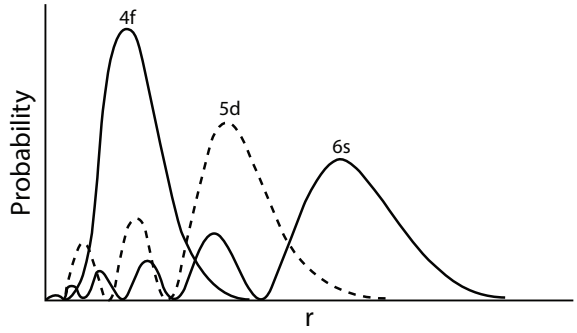

Figure 3-1: Probability to find 4f, 5d and 6s electrons on a distance *r* from the nucleus of a lanthanide. Note that the 4f orbitals are strongly shielded by the 5s and 6p orbitals. Adapted from Cotton.[1]

Table 3-1: Electron configurations of the lanthanides and the corresponding trivalent oxidation state.

Element	Ln^0	Ln^{3+}
La	[Xe] $5d^1$ $6s^2$	[Xe]
Ce	[Xe] $4f^1$ $5d^1$ $6s^2$	[Xe] $4f^1$
Pr	[Xe] $4f^3$ $6s^2$	[Xe] $4f^2$
Nd	[Xe] $4f^4$ $6s^2$	[Xe] $4f^3$
Pm	[Xe] $4f^5$ $6s^2$	[Xe] $4f^4$
Sm	[Xe] $4f^6$ $6s^2$	[Xe] $4f^5$
Eu	[Xe] $4f^7$ $6s^2$	[Xe] $4f^6$
Gd	[Xe] $4f^7$ $5d^1$ $6s^2$	[Xe] $4f^7$

Element	Ln^0	Ln^{3+}
Tb	[Xe] $4f^9$ $6s^2$	[Xe] $4f^8$
Dy	[Xe] $4f^{10}$ $6s^2$	[Xe] $4f^9$
Ho	[Xe] $4f^{11}$ $6s^2$	[Xe] $4f^{10}$
Er	[Xe] $4f^{12}$ $6s^2$	[Xe] $4f^{11}$
Tm	[Xe] $4f^{13}$ $6s^2$	[Xe] $4f^{12}$
Yb	[Xe] $4f^{14}$ $6s^2$	[Xe] $4f^{13}$
Lu	[Xe] $4f^{14}$ $5d^1$ $6s^2$	[Xe] $4f^{14}$

Spectroscopic properties of lanthanides

Last decades, extensive research has been carried out to explain the electronic transitions of lanthanides. It was found that the transitions between the various $4f^n$ states, the so-called $4f^n$ - $4f^n$ transitions, are very well-defined and have features resembling those of free ions. Especially, they do not vary much with the chemical environment when inserted into different host materials (*e.g.* from $NaYF_4$ to Y_2O_3).[cotton,blasse] Therefore, the energy levels of all lanthanides were measured in the crystal lattice LaF_3 and can now be found in the so-called Dieke diagram, shown in Figure 3-3.[blasse] The host material LaF_3 is a low-symmetry crystal and is a good reference since crystal field splitting is almost absent (usually less than 100 cm^{-1}). The thicknesses of the energy levels in the diagram correspond to the degree that energy levels are affected by the crystal field.

The well-defined transitions of lanthanides can be explained by the configurational coordinate diagram. Moreover, the luminescence of d-block metals will be shortly discussed to compare the luminescence with that of lanthanides. Figure 3-2 shows the coordinate diagrams of a lanthanide and a d-block metal.[cotton] In both cases, a photon can be adsorbed to promote the ion from the ground state (GS) to the excited state (ES), indicated by upward arrows in the Figure.

For lanthanides, the change in distance between atoms and ligands upon excitation is negligible by the shielding of the f-orbitals by the 5s and 5p orbitals. Therefore, the Stokes' shift (ΔS), the change in distance between the atom and the ligand upon excitation of the luminescent center, is neglegible. Emission consequently arises from the ES to the GS at an equal wavelength as absorption, yielding overlapping excitation and emission peaks.

For d-block metals, the metal-ligand distance strongly increases upon excitation, resulting in large Stokes' shifts since the d-block orbitals are not shielded. Non-radiative relaxation occurs, yielding emission at much longer wavelengths, as visualized in the combined excitation and emission spectrum in Figure 3-2. Important parameters affecting the Stokes' shift are the presence of ligands and the nephelauxatic effect.

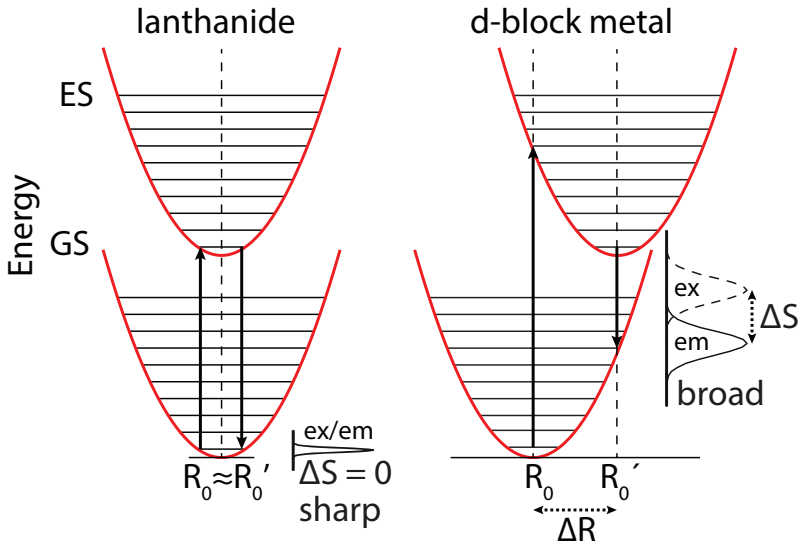

Figure 3-2: Configurational diagrams for a lanthanide (left) and a d-block metal (right) with corresponding excitation and emission spectra.

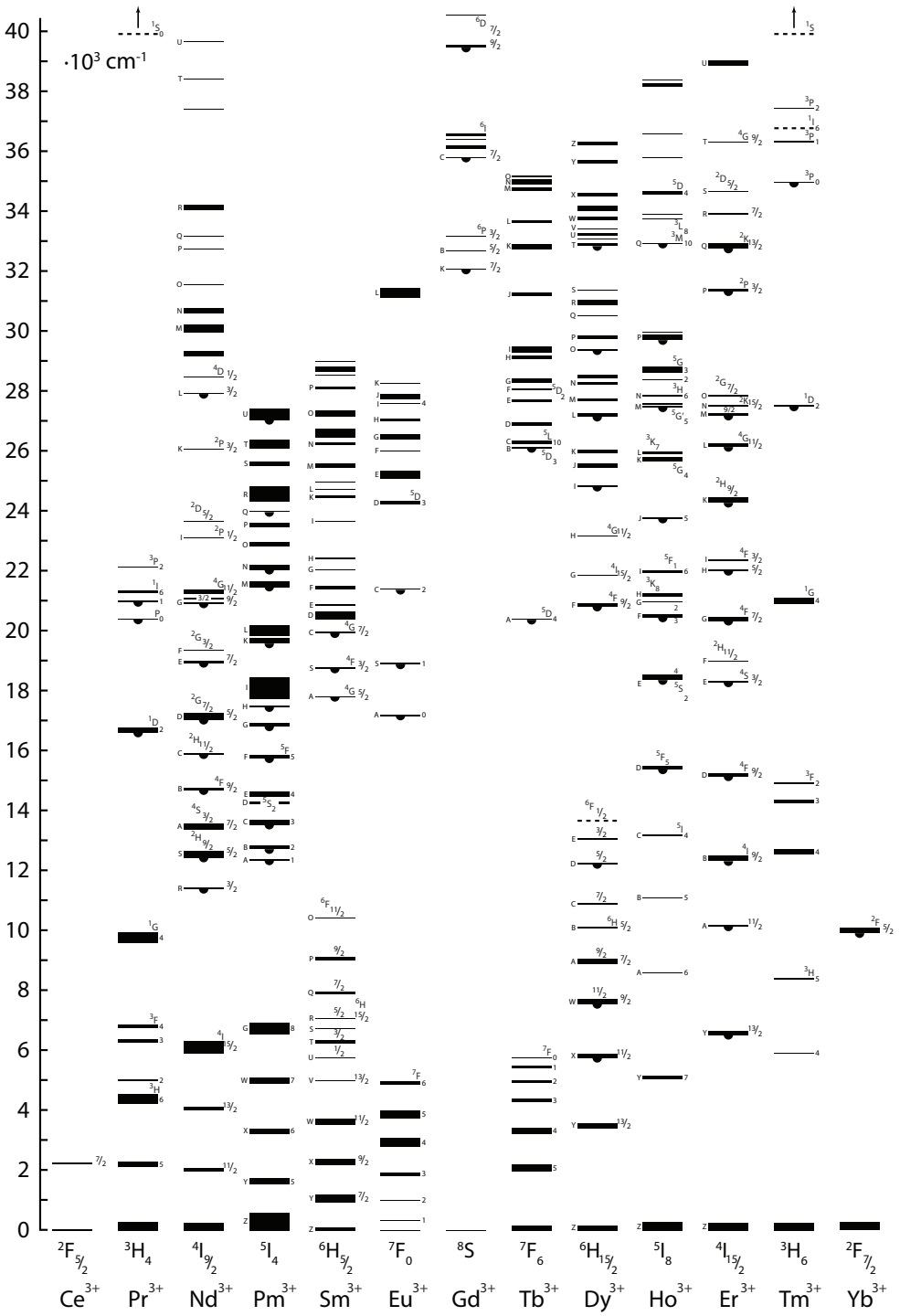

Figure 3-3: The Dieke diagram, the energy levels of Ln^{3+}-series measured in the crystal lattice LaF_3, adapted from the work of M. de Jong.[3,4]

Energy levels and term symbols

The various electron distributions over the 4f-orbitals are the origin of the microstates in lanthanides. [2] The number of possible electron distributions can be calculated by taking the number of orbitals $n = 14$ and the orbital quantum number $l = 3$ into account:

$$\frac{(4l+2)!}{n!(4l+2-n)} = \frac{14!}{n!(14-n)!} \text{ if } l = 3. \qquad \text{Equation 3-1}$$

For instance, 2002 microstates are available for Tb^{3+}, an $4f^9$-ion.

Figure 3-4 shows a schematical depiction of energy splitting in lanthanides which forms the energy levels. The electrons are distributed over the atomic orbitals which results in the $4f^n$ ground state. The energy needed for excitating an $4f^n$ electron to the higher-lying 5d orbital, resulting in the $4f^{n-1}5d^1$ excited state, is in the order of 10^4 cm^{-1}.

The splitting of the $4f^n$ orbitals into multiple energy levels arises by four different causes. Firstly, the $4f^n$ level splits into $2J+1$ ^{2S+1}L levels by interelectronic repulsion of electrons and is called the free electron state. The symbols *S, L* and *J* denote respectively the total spin moment, the total orbital angular moment and the total angular momentum (*i.e.* the vector sum of *S* and *L*). The values of *L* are designated by the letters S, P, D, F, G, H, I, K and L for *L*=0, 1, 2, 3, 4, 5, 6, 7 and 8, respectively.[1]

Secondly, further splitting by spin-orbit coupling, also called Russell-Saunders coupling, generates $2J+1$ energy levels which are assigned by the Russel-Saunders term symbols $^{2S+1}L_J$. Thirdly, the energy states of a lanthanide are also affected by the electric field of the ligand or crystal, although this influence is limited. Each $^{2S+1}L_J$ energy state is split into various energy levels with maximal energy differences of about 200 cm^{-1} which corresponds to the thicknesses of energy levels in the Dieke diagram. Fourthly, external magnetic or electric fields can split the *J*-values further. However, this influence on lanthanides is very small since the energy variations are in the order of 1 cm^{-1}.

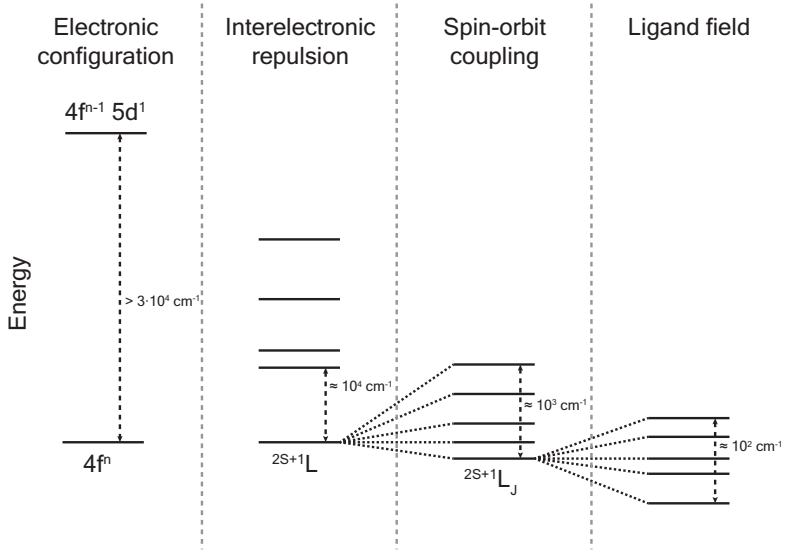

Figure 3-4: Schematical illustration of the energy splitting of lanthanides. The $4f^n$ energy levels are splitted by electronic repulsion, spin-orbit coupling and the ligand field, respectively.[1]

The ground state term symbol of an ion after spin-orbit coupling can be determined using Hund's rules. First, the greatest spin multiplicity S lies lowest in energy. If there is more than one term with equal spin multiplicity, the term containing the highest L value is the ground state. If there is more than one term containing the same L as ground state the J-value has to be taken into account. For a shell which is less than half-filled, the J term with the lowest value is the ground term. In contrast, if the f-orbitals are half-filled or more, the ground state contains the highest value of J.

For instance, Eu^{3+}, with an f^6-configuration has a ground state labeled $^7F_0$. The 6 electrons can be placed parallel in the orbitals with highest angular momentum, resulting in $S = 3$ and $L = 3$. By applying the Russel-Saunders term symbols, this results in ^7F_J, with J ranging from 0 to 6. Since the orbitals are less than half filled, the lowest energy level is the $^7F_0$ level.

Types of electronic transitions

Most lanthanides can absorb and emit photons in UV, visible and/or NIR regions. These absorptions and emissions arise by three types of electronic transitions: sharp intra-configurational $4f^n$ - $4f^n$ transitions (transitions between the $4f^n$ energy levels from the Dieke diagram), broader 4f-5d transitions and broad charge-transfer (CT) transitions.[5] CT involves the transfer of charge from metal-to-ligand (MLCT) or ligand-to-metal (LMCT). The 4f-5d and CT transitions are of a higher intensity since they are parity allowed and occur at higher energies than than that $4f^n$-$4f^n$ transitions (usually at wavelengths smaller than 300 nm) and appear as broad bands. However, not all these transitions are allowed by the Laporte selection rule which dictates that transitions with the same initial and final parity are forbidden.

Intra-configurational $4f^n$ - $4f^n$ transitions are allowed if the matrix element for an electronic transition $< \Psi_i |O| \Psi_f >$ is nonzero, i and f are the initial and final wavefunctions whearas O is the transition operator. The physical interpretation of this rule is that transitions with the same parity are forbidden because according to quantum mechanics, the parity should be inverted after the transition. The probability for an absorption or emission is expressed as the oscillator strength with a value between 0 and 1.[5] The intensity of peaks in absorption and emission spectra can be explained by the selection rules and oscillator strengths.

The $4f^n$ - $4f^n$ transitions could arise by four types of transitions, namely the Judd forced electric dipole (ED, also called induced ED), magnetic dipole (MD), electric quadrupole (EQ) and one phonon ED vibronic transitions.[tanner] The four transition types are listed with their selection rules and oscillator strengths in Table 3-2. The Judd forced ED and MD transitions are the most important transitions for sharp $4f^n$ - $4f^n$ transitions because of their relative high oscillator strengths, resulting in intense transitions. ED and MD transitions get their intensity by the mixture of higher electronic states of opposite parity. Mixing arises by the presence of a low-symmetric crystal field or by asymmetric molecular vibrations which temporarily lift the symmetry.

However, the La^{3+} and Lu^{3+} lanthides do not exhibit $4f^n$ - $4f^n$ transitions since both ions have very stable [Xe] $5d^1$ $6s^2$ and [Xe] $4f^{14}$ $5d^1$ $6s^2$ configurations, respectively.[cotton] Furthermore, Gd^{3+} has no transitions in visible and NIR wavelength regions because it has a very stable [Xe] $4f^7$ $5d^1$ $6s^2$ configuration.

Table 3-2: Selection rules for electronic transitions of trivalent lanthanides.[5]

Type of transition	J selection rules	Oscillator strength
Electric dipole (ED)	$\|\Delta J\| \leq 1$ with $J \neq J' = 0$ is forbidden	0.01-1
Judd forced ED	$\|\Delta J\| \leq 6$ if $J = 0$, or $J' = 0$ if $\|\Delta J\| = 2,4,6$	10^{-4} of ED
Magnetic dipole (MD)	$\|\Delta J\| \leq 1$ with $J = J' = 0$ is forbidden	10^{-6} of ED
Electric quadrupole (EQ)	$\|\Delta J\| \leq 2$ with $J = 0$ and $J' = 0, 1$ are forbidden	10^{-10} of ED
One phonon ED vibronic	equal to Judd forced ED	10^{-7} - 10^{-10} of ED

Decay of excited states

After the excitation of a lanthanide ion to an excited state, various pathways are available for a luminescent center to return to the ground state which occurs either radiatively (as discussed previously) or non-radiatively. The relaxation is strongly coupled to the surroundings of the luminescent ions, *e.g.* solvents, ligands, defects and neighbouring ions. Here, the most important non-radiative decay processes will be discussed shortly.

The first process, multi-phonon relaxation, is a major non-radiative decay pathway. An excited luminescent center can transfer its energy to phonons of the host material, the collective oscillation of atoms, resulting in the quenching of energy. However, if the energy difference between two adjacent energy levels requires the energy of 5 phonons or more, the dominant decay mechanism for that specific energy level is radiative. In other words, the luminescence of an energy level is less efficient if the energy gap to a lower-lying energy level could be bridged by 5 phonons.[2]

In this study, Y_2O_3 has been chosen as host material to incorporate luminescent lanthanides since it exhibits a relatively low phonon energy ν_{max} of ~600 cm^{-1}, resulting in small non-radiative decay rates.[2] This is in contrast to other host materials such as the silicates, borates and phosphates where ν_{max} values between 1000 and 1200 cm^{-1} are observed which could bridge the energy gap between two energy levels more efficiently, leading to high non-radiative decay rates.[2]

Another major decay process is concentration quenching.[2] This process arises by the loss of energy to defects in the crystal lattice at relatively high dopant concentrations. The energy of an excited center can migrate over the lattice via neighbouring centers until a defect is encountered which quenches the energy. Examples of defects are vacancies, defects and lattice mismatches. This quenching process can be reduced by lowering the dopant concentrations, resulting in the can quench the luminescence by absorbing the energy and dissipating the energy non-radiatively.

Upconversion of Er^{3+} by Yb^{3+}

Upconversion is anti-stokes emission with emission at shorter wavelengths than excitation. In this process, two low-energetic photons are combined into one high-energetic photon. A well-known upconversion couple is Er^{3+}/Yb^{3+}, in which Yb^{3+} acts as sensitizer for the activation of Er^{3+}. Low-energetic infrared photons are absorbed and emitted as high-energetic green photons. Although it has been demonstrated that single-doped Er^{3+} samples are capable of upconversion, the low absorption cross section of Er^{3+} results in very poor emission. Therefore, Yb^{3+} is incorporated to activate Er^{3+}.

The activation of Er^{3+} via upconversion has multiple advantages over direct excitation. Firstly, the clear separation of the excitation and emission wavelengths reduces scattering effects in the visible emission region. Secondly, IR photons penetrate deeper in solid and liquid media than UV or visible photons.

Various pathways have been proposed for the upconversion processes and are depicted in Figure 3-6. [6-9] The first pathway is the excitation of erbium by excitated state absorption (ESA). Erbium is excited by the uptake of two photons from the $^4I_{15/2}$ ground state to $^4I_{11/2}$ and consequently further excited to the $^4F_{7/2}$ state. The second pathway is energy transfer upconversion (ETU) where two excited erbium $^4I_{15/2}$ neighbouring interact. Both ions are excited by ground state absorption under the uptake of a 980 nm photon. One ion absorbs the energy of the other and is excited to the $^4F_{7/2}$ whereas the other is de-excited to the $^4I_{15/2}$ ground state. Although both pathways have been observed in single-doped Er^{3+}-samples, the emission is poor since the absorption cross-section of Er^{3+} at 980 is very low.

Nevertheless, the third pathway results in high Er^{3+} emission intensity and is a two-step energy transfer (two-step ET) process from neighbouring ytterbium ions to erbium. In the first step of the process, two ytterbium ion are excited from the $^2F_{7/2}$ to the $^2F_{5/2}$ energy level by the adsorption of two 980 nm photons. ET from ytterbium to erbium takes place what results in the excitation of erbium from the $^4I_{15/2}$ ground state to the $^4I_{11/2}$ energy level. A second ET follows and erbium is further excited from the $^2I_{11/2}$ to the $^4F_{7/2}$ energy level.

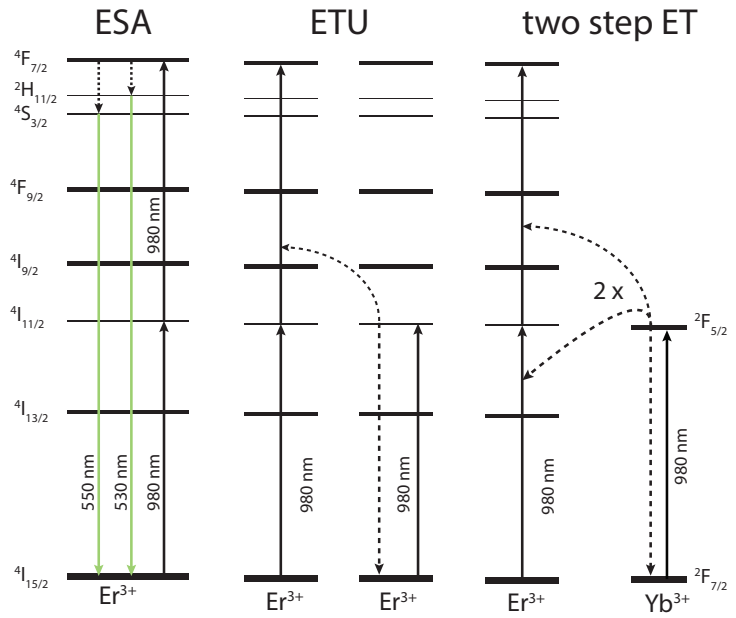

Figure 3-6: Schematic representation of the upconversion processes excited state absorption (ESA), energy transfer upconversion (ETU) and two step energy transfer (ET) of the Er^{3+}/Yb^{3+}-couple upon excitation at 980 nm.

Thermal coupling of energy levels and the fluorescence intensity ratio method

In 1976, Kusuma et al. proposed a method to determine the temperature from the luminescence of lanthanides.[10] If two energy levels are closely spaced, *e.g.* exhibit an energy difference of approximately 1,000 cm^{-1} or several k_BT, the populations are thermally coupled by a Boltzmann distribution. The thermal energy available at room temperature is sufficient to bridge this energy gap and to set the thermal distribution.

In this research, the lanthanide ions Eu^{3+}, Dy^{3+} and Er^{3+} are exploited which contain differences between the energy levels of 1,700 cm^{-1}, 1,000 and 750 cm^{-1}, respectively.[3,4] In Figure 3-7 the energy levels are shown with the thermally coupled energy levels placed in red boxes. From the variation in energy difference, it is expected to find different temperature dependent regions, *i.e.* the energy difference of Er^{3+} is smaller than that of Eu^{3+} which result in temperature dependence at lower temperatures.

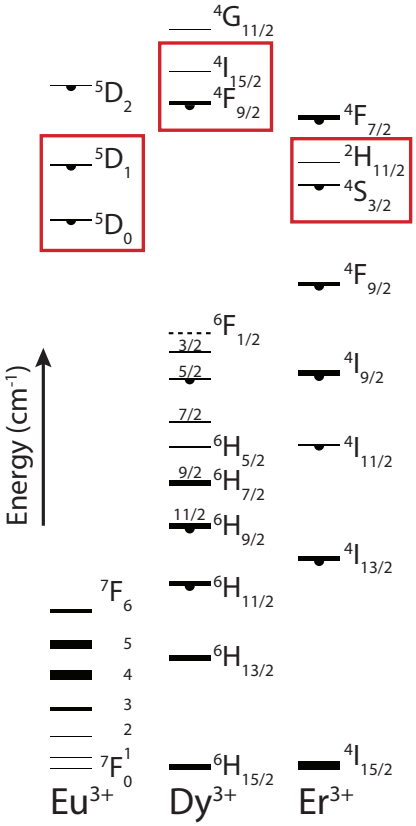

Figure 3-7: Energy levels diagrams of the lanthanide Eu^{3+}, Dy^{3+} and Er^{3+} ions. The thermally coupled energy levels are placed in red boxes.[3,4]

Assume a system with four energy levels, shown in Figure 3-8. The system is excited from the ground state (GS) to the higher lying energy level, indicated by the blue arrow. Non-radiative relaxation takes place to the radiative energy levels 1 and 2. Since the energy difference between energy level 1 and 2 is approximately of 200 cm^{-1}, the energy levels are thermally coupled and therefore the populations in the excited states 1 and 2 follow a Boltzmann distribution.[10] Afterwards, the temperature is determined from the radiative decay of these levels to the GS.

The intensity, I_i, from the decay of level 1 and 2 to the ground state is described as

$$I_1(T) = p_1 N_1(T) \text{ and } I_2(T) = p_2 N_2(T). \qquad \text{Equation 3-2}$$

p_i is the transition probability, the chance to decay from state i to the ground state, and $N_i(T)$ is the level population at temperature T. The temperature of a certain object can be determined by calculating the fluorescence intensity ratio (FIR) of the energy level populations.

$$FIR = \frac{I_2(T)/I_1(T)}{I_2(T_0)/I_1(T_0)} = \frac{p_2 N_2(T)/p_1 N_1(T)}{p_2 N_2(T_0)/p_1 N_1(T_0)} = \frac{N_2(T)/N_1(T)}{N_2(T_0)/N_1(T_0)} \qquad \text{Equation 3-3}$$

After rearranging the equation, the FIR is only dependent of the relative level populations at the two temperatures. If the system is in equilibrium and if the energy separation is in the order of a few k_BT, the ΔE_{21}, is independent of the temperature then the populations N_1 and N_2 are related by the Boltzmann factor:

$$\frac{N_2(T)}{N_1(T)} = exp\left(-\frac{\Delta E_{21}}{k_B T}\right) \qquad \text{Equation 3-4}$$

The unknown temperature T can be determined from the FIR and the known reference temperature T_0

$$T = \left[\frac{1}{T_0} - \frac{k}{\Delta E_{21}} lnR\right]^{-1}. \qquad \text{Equation 3-5}$$

Via equation 3.2 and 3.4 we can make equation 3.6. Note that the ratio p_2 over p_1 is just a constant.

$$ln\left(\frac{I_2}{I_1}\right) = ln\left(\frac{p_2}{p_1}\right) - \frac{\Delta E_{21}}{k_B T} = lnA - \frac{\Delta E_{21}}{k_B T} \qquad \text{Equation 3-6}$$

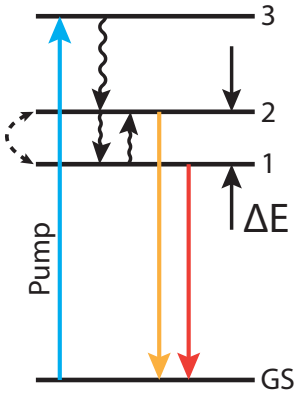

Figure 3-8: Schematical representation of the thermal coupling of two energy levels, resulting in temperature dependent emission.

An example of such a temperature dependence can be found in Figure 3-9 (a) where two emission spectra for Er^{3+}/Yb^{3+} at 300 and 900 K are depicted.[7] At 300 K (green spectrum) the lowest state from the thermally coupled states, $^4S_{3/2}$, is more occupied than the higher state $^2H_{11/2}$, resulting in more emission from $^4S_{3/2}$ than from $^2H_{11/2}$. At 900 K (blue spectrum) the $^2H_{11/2}$ state is more filled than the lower state which results in more emission from the $^2H_{11/2}$-state. If the reciprocal temperature is plotted versus the logarithm of the intensity ratio of two emission peaks, we should find a straight line as expected from Equation 3-6. In Figure 3-9 (b) this is done for the Er^{3+}/Yb^{3+}-couple by exploiting the emission bands at 523 and 548 nm between 300 and 900 K.[7]

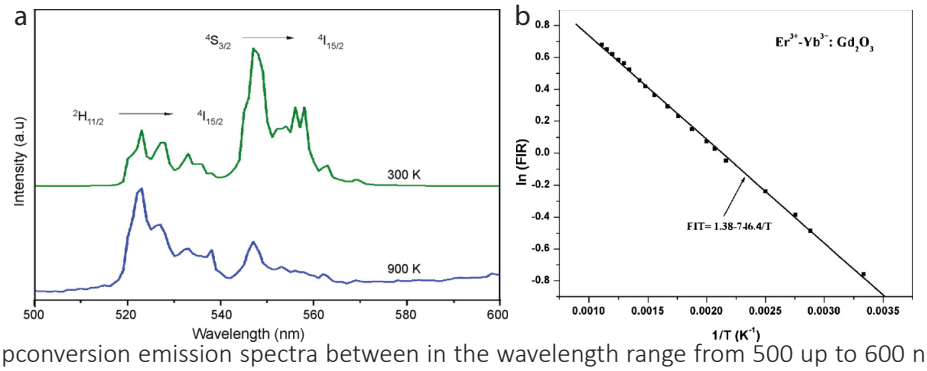

Figure 3-9: (a): Upconversion emission spectra between in the wavelength range from 500 up to 600 nm of Er^{3+}/Yb^{3+} in Gd_2O_3 at 300 K (top) and 900 K (bottom) upon excitation at 976 nm. b: Calculated temperature depence from the emission spectra. Adapted from [singh].

3.3 Methods

Luminescence spectra at room temperature were recorded on an Edinburgh Instruments FL900 spectrophotometer equipped with a Xe-lamp as excitation source and a R9288 PMT photon dector. Luminescence measurements, other than at room temperature, were performed in a temperature controlled cell from Linkam Scientific Instruments adjustable from room temperature up to 600 °C. Temperature dependent spectra of Dy^{3+}-doped samples were recorded with the FL900 set-up whereas samples of Eu^{3+} and Er^{3+}/Yb^{3+} (co-)doped samples were measured with a CCD camera of Ocean Optics QEPRO. Eu^{3+} and Er^{3+}/Yb^{3+} (co-)doped samples were excitated with a hand-held portable UV lamp (λ_{exc} = 254 nm) and a 2W diode laser (λ_{exc} = 980 nm), respectively.

3.4 Results and discussion

1. Luminescence of Y_2O_3:Eu^{3+} NPs and deposition on α-Al_2O_3

To investigate the luminescence properties of the Y_2O_3:$Eu_{0.05}$ NPs, room temperature excitation and emission measurements were performed. The results shown in Figure 3-10. All measurements were performed using a Xenon lamp as excitation source. Figure 3-10 (a) shows the excitation spectrum upon fixed emission at 611 nm. In the emission region between 240 nm and 500 nm a broad absorption band is found at 260 nm and two distinct groups of peaks around 395 nm and 460 nm. The absorption band at 260 nm is ascribed to the charge transfer band (CTB) between O^{2-} to Eu^{3+} ions. [11] This observation confirms that both Eu^{3+} and O^{2-} atoms are incorporated in the lattice. The two groups of peaks correspond to the $^7F_0 \rightarrow {}^5L_6$ and $^7F_0 \rightarrow {}^5D_2$ transitions of Eu^{3+}, respectively.

Figure 3-10 (b) shows the emission spectrum of Y_2O_3:$Eu_{0.05}$ NPs under excitation at 258 nm. In the emission range from 450 nm up to 750 nm numerous peaks of Eu^{3+} are observed. The peak located at 580 nm and the group of peaks at 586, 593 and 599 nm arise by the $^5D_0 \rightarrow {}^7F_0$ and $^5D_0 \rightarrow {}^7F_1$ transitions, respectively. The most intense emission peak at 611 nm with a shoulder at 630 nm, is attributed to the $^5D_0 \rightarrow {}^7F_2$ transition. The two groups of weaker peaks around 655 nm and 710 nm correspond to the $^5D_0 \rightarrow {}^7F_3$ and $^5D_0 \rightarrow {}^7F_4$ transitions, respectively.

To examine the deposition of Y_2O_3:$Eu_{0.05}$ NPs on α-Al_2O_3 on the luminescence, similar measurements as in Figure 3-10 were performed on a sample of 5 wt% Y_2O_3:$Eu_{0.05}$ NPs / α-Al_2O_3. The results are shown in Figure 3-11. As can be seen, the excitation and emission spectra of 5 wt% Y_2O_3:$Eu_{0.05}$ NPs / α-Al_2O_3 complexes are identical to the spectra of Y_2O_3:$Eu_{0.05}$ NPs. From this, it can be concluded that there is no influence from α-Al_2O_3 on the luminescence of the Y_2O_3:$Eu_{0.05}$ NPs.

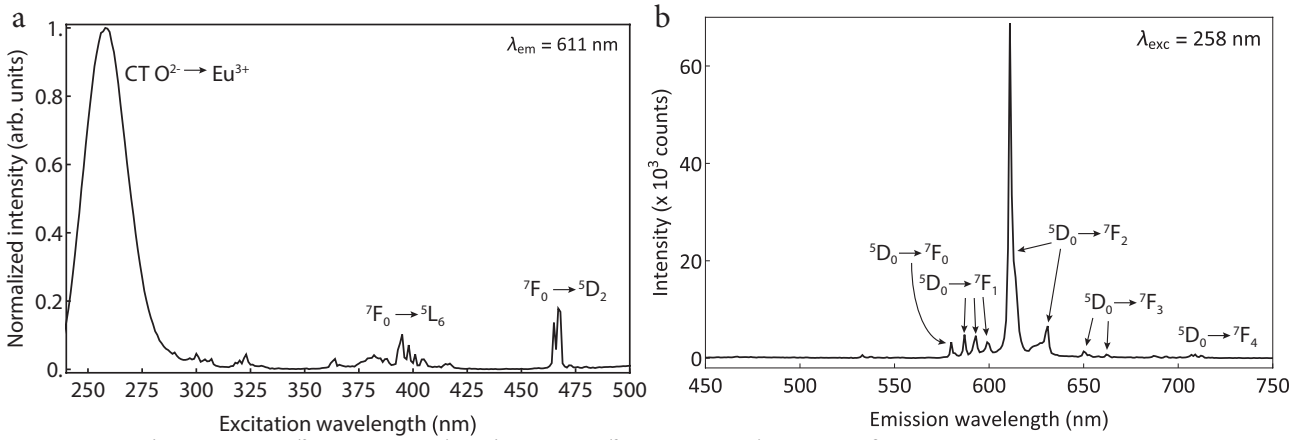

Figure 3-10: The excitation (λ_{em} = 611 nm) and emission (λ_{exc} = 258 nm) spectra of Y_2O_3:$Eu_{0.05}$ NPs.

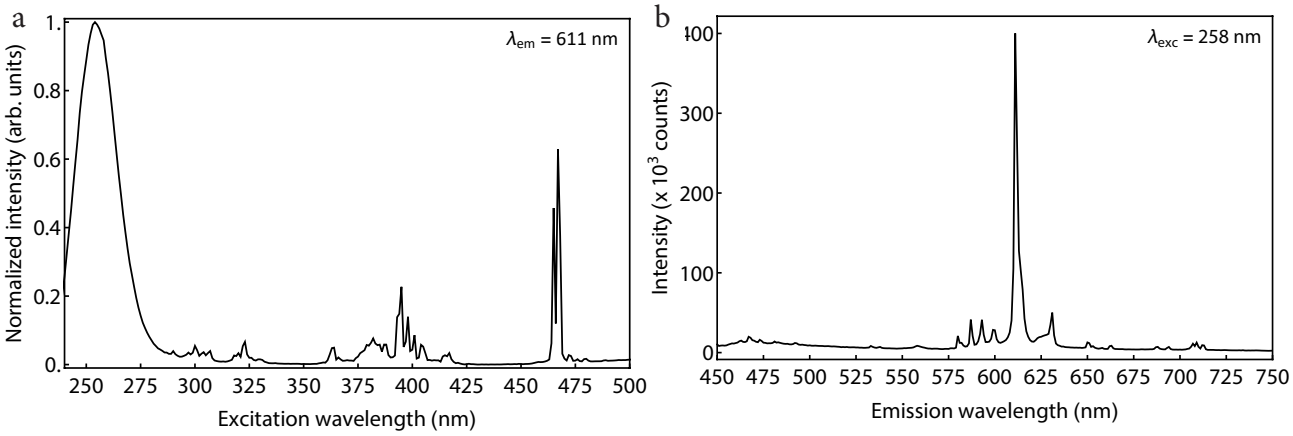

Figure 3-11: The excitation (λ_{em} = 611 nm) and emission (λ_{exc} = 258 nm) spectra of 5 wt% Y_2O_3:$Eu_{0.05}$ NPs / α-Al_2O_3.

2. Temperature-dependent luminescence of 5 wt% Y_2O_3:$Eu_{0.05}$ NPs / α-Al_2O_3

In order to investigate the applicability of Y_2O_3:$Eu_{0.05}$ NPs on α-Al_2O_3 as temperature probes, temperature dependent luminescence measurements were performed on the sample of 5 wt% Y_2O_3:$Eu_{0.05}$ NPs / α-Al_2O_3. The measurements were performed by excitating the samples at 254 nm while monitoring emission between 520 and 670 nm as shown in Figure 3-12. The temperature was increased from room temperature (blue spectrum) up to 600 °C (red spectrum) with intervals of 25 °C. Multiple peaks are observed which are equivalent to those of Figure 3-11 (b). In addition, at elevated temperatures two groups of peaks arise around 530 nm and 550 nm which correspond to the $^5D_1 \rightarrow {}^7F_1$ and $^5D_1 \rightarrow {}^7F_2$ transitions, respectively. The intensity ratio of the $^5D_1 \rightarrow {}^7F_{1,2}$ versus $^5D_0 \rightarrow {}^7F_{0,1,2,3}$ transitions increases with increasing temperature as expected by the thermal coupling from the populations of the $^5D_0$ and $^5D_1$ excited states.

To investigate the temperature dependent fluorescence intensity ratio further, the natural logarithm of the integrated intensity ratio is plotted versus $1/T$, as shown in Figure 3-13. A non-linear relation of the FIR versus $1/T$ is observed between room temperature and 225 °C. This dependence can be explained by a combination of two processes: multi-phonon relaxation and thermal coupling of the $^5D_0$ and $^5D_1$ excited states. From room temperature up to 100 °C, the FIR decreases with increasing temperature by the rise of multi-phonon relaxation. Multi-phonon relaxation is correlated to the temperature and increases the relaxation from the $^5D_1$ to the $^5D_0$ energy state what consequently enhances the $^5D_0 \rightarrow {}^7F_{0,1,2,3}$ emission with increasing temperature. In the temperature range from 100 °C up to

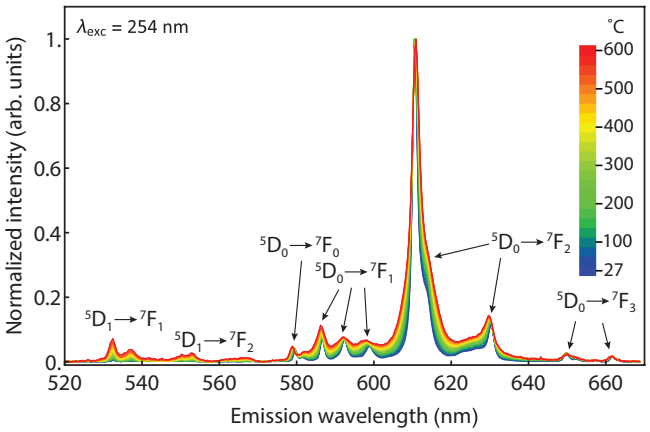

Figure 3-12: Temperature dependent emission spectra of 5 wt% Y_2O_3:$Eu_{0.05}$ / α-Al_2O_3 upon excitation at 254 nm between room temperature and 600 °C in steps of 25 °C, normalized at 611 nm.

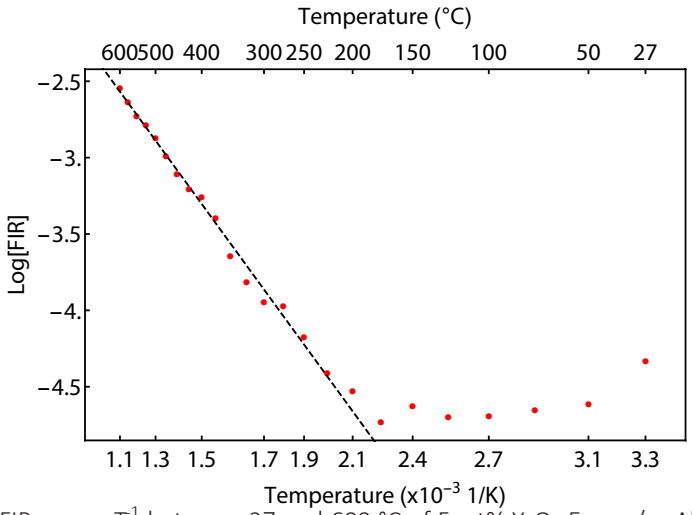

Figure 3-13: Logplot of the FIR versus T^{-1} between 27 and 600 °C of 5 wt% Y_2O_3:$Eu_{0.05}$ / α-Al_2O_3. The intensity ratio was calculated by dividing the integrated area between 521-571 nm and 571-660 nm. The linear model was fitted between 225 and 600 °C with a calculated coefficient of determination (R^2) of 0.9929.

225 °C, the FIR gradually increases with increasing temperature. The thermal coupling starts to exert a major influence over the multi-phonon relaxation and results in a slight increase of the FIR.

Between 225 and 600 °C the experimental data can be fitted to a linear model, as expected from Equation 3-6. The coefficient of determination (R^2) was calculated to be 0.9927, indicating a satisfactory relation of the experimental data to the model fit. From the slope of the line an energy difference between the $^5D_0$ and $^5D_1$ energy levels was found to be 1501 cm^{-1} which is in the same order as deduced from the Dieke diagram which is approximately 1700 cm^{-1}.[3]

For temperature sensing applications, it is required that the temperature probes are accurate and durable. Therefore, thermal cycling experiments were carried out between 225 and 600 °C. Figure 3-14 (a) shows the recorded emission spectra at 225, 375, 450 and 600 °C for four temperature cycles between 225 and 600 °C. Identical emission spectra were found, suggesting reproducible temperature measurements without decay of emission intensity during the cycling experiments.

To examine the accuracy of the probes, the temperature was calculated from the spectra by exploiting the model fit from Figure 3-13, the results are shown in Figure 3-14 (b). Identical temperatures during the cycles were found confirming the durability of the temperature probes. The accuracy of the temperature probes was determined by calculating the standard deviations of the calculated temperatures. Accuracies of 12.1, 8.8, 5.6 and 8.0 °C were found for the measurements performed at 225, 350, 475 and 600 °C, respectively.

The relatively low accuracy arises from two different reasons. Firstly, only a small change from the $^5D_0 \rightarrow {}^7F_{0,1,2,3,4}$ versus $^5D_1 \rightarrow {}^7F_{1,2}$ transitions with changing temperature is observed which results in relatively large measurement errors. Secondly, the weak emission from the $^5D_1 \rightarrow {}^7F_{1,2}$ transitions exhibits a low signal to noise ratio which lowers the accuracy significantly.

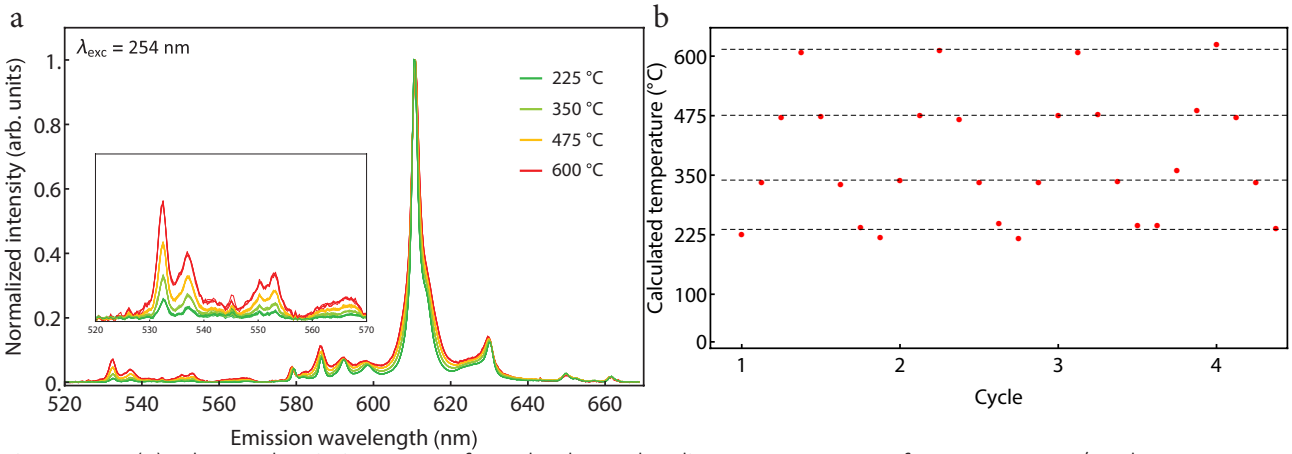

Figure 3-14: (a): Observed emission spectra from the thermal cycling measurements of Y_2O_3:$Eu_{0.05}$ NPs / α-Al_2O_3 at temperatures of 100, 225, 350 and 475 °C, normalized at 611 nm. (b): Calculated temperatures for every spectrum by exploiting the fluorescence intensity ratio. The dashed lines indicate the average calculated temperature.

3. Luminescence Y_2O_3:$Dy_{0.0085}$ NPs and deposition on α-Al_2O_3

To investigate the luminescent properties of the Y_2O_3:$Dy_{0.0085}$ NPs, excitation and emission spectra were recorded at room temperature. Figure 3-15 (a) shows the excitation spectrum with fixed emission at 572 nm. Multiple groups of sharp peaks appear which are similar to the observations of Dominiak et al..[12] The strongest absorption peak is located at 350 nm and corresponds to the $^6H_{15/2}\rightarrow{}^6P_{7/2}$ transition whereas the group of weaker peaks between 375 and 400 nm arises by the $^6H_{15/2}\rightarrow{}^4M_{21/2}$,$^4I_{13/2}$,$^4F_{5/2}$ transitions, respectively. The peaks at 425 and 450 nm arise by the $^6H_{15/2}\rightarrow{}^4G_{11/2}$ and $^6H_{15/2}\rightarrow{}^4I_{15/2}$ transitions, respectively.

The emission spectrum, depicted in Figure 3-15 (b), under fixed excitation at 353 nm shows two groups of peaks at 480 and 570 nm which arise by the emission from the $^4F_{9/2}\rightarrow{}^6H_{15/2}$ and $^4F_{9/2}\rightarrow{}^6H_{13/2}$ transitions.[12] No peak at 455 nm is visible were the $^4I_{15/2}\rightarrow{}^6H_{15/2}$ transition is expected to occur by the coupling of the $^4I_{15/2}$ and $^4I_{15/2}$ energy levels at elevated temperatures.[13]

Similar excitation and emission spectra were recorded for the sample containing 5 wt% Y_2O_3:$Dy_{0.0085}$ NPs / α-Al_2O_3 to investigate the effect of α-Al_2O_3 on the luminescence, shown in Appendix 3.7.1. Although the luminescence is decreased after deposition on α-Al_2O_3, the $^4F_{9/2}\rightarrow{}^6H_{15/2}$ transition is clearly observed which is required for temperature probing.

4. Temperature dependent luminescence of Y_2O_3:$Dy_{0.0085}$ NPs / α-Al_2O_3 and Y_2O_3:$Dy_{0.0085}$ NPs

In order to study the temperature-dependent emission of 5 wt% Y_2O_3:$Dy_{0.0085}$ NPs / α-Al_2O_3, temperature dependent luminescence measurements were performed. Emission spectra were recorded between 440 and 510 nm upon excitation at 350 nm. The temperature was increased from room temperature (blue spectrum) to 600 °C (red spectrum), the results are shown in Figure 3-16 (a). At all temperatures a strong declining background is visible which arises by scattering effects of α-Al_2O_3. These effects could be minimized by shifting the excitation wavelength to shorter wavelengths. However, this is not feasible for this system since there are no strong adsorption peaks of Dy^{3+} in the deeper UV region.

Although the declining background plays a major role in the emission spectra, the emission of the $^4I_{15/2}\rightarrow{}^6H_{15/2}$ transition between 440 nm 470 nm is clearly observable above 300 °C. Furthermore. the emission of the $^4F_{9/2}\rightarrow{}^6H_{15/2}$ transition in the wavelength range of 470 nm up to 510 nm is already visible at room temperature and slightly decreases at higher temperatures. The increase of the emission originating from the $^4I_{15/2}$ and decrease of the emission originating from the $^4F_{9/2}$ level indicates thermal coupling of these two energy levels.

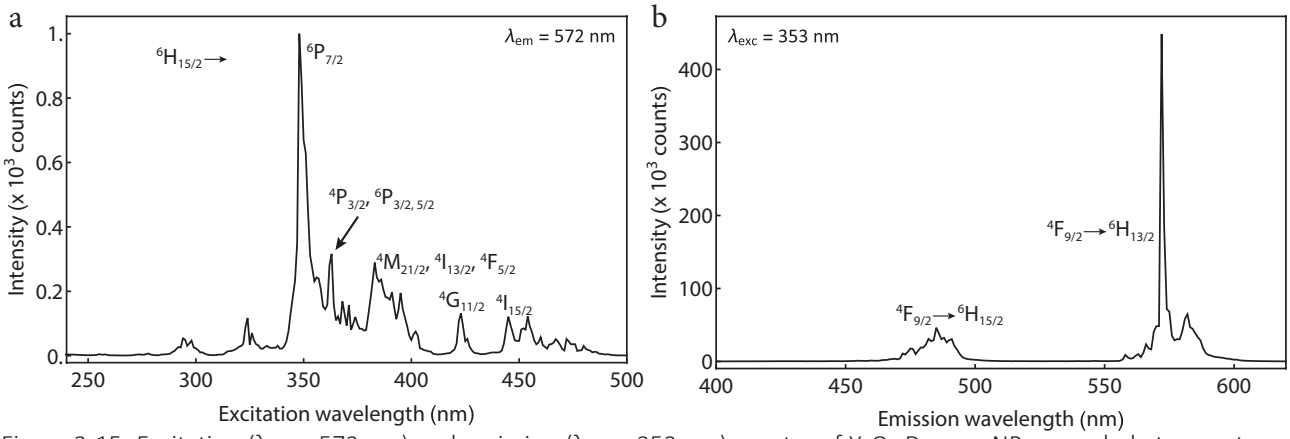

Figure 3-15: Excitation (λ_{em} = 572 nm) and emission (λ_{exc} = 353 nm) spectra of Y_2O_3:$Dy_{0.0085}$ NPs recorded at room temperature.

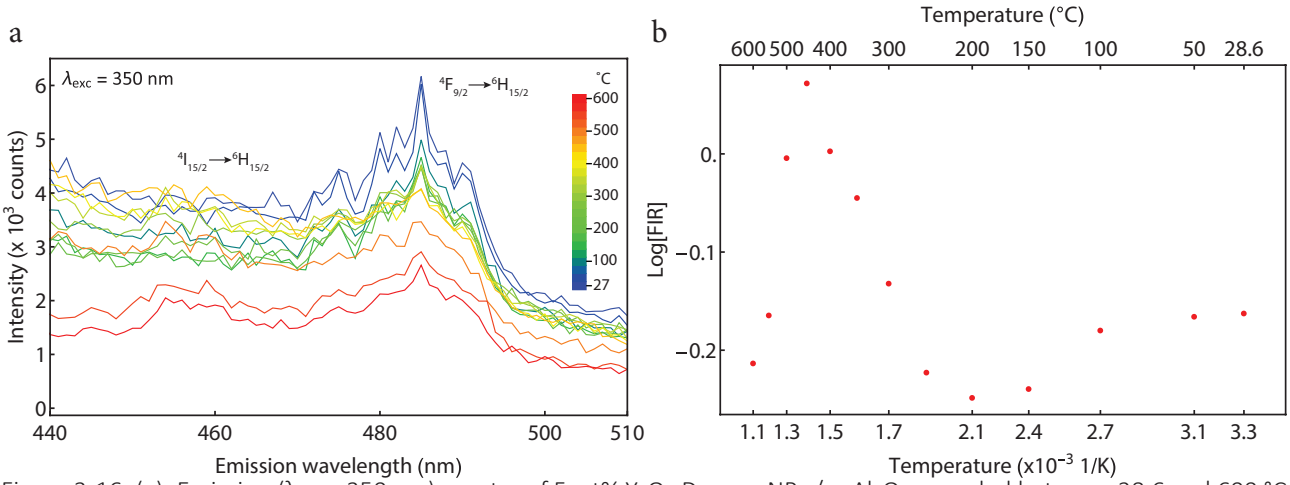

Figure 3-16: (a): Emission (λ_{exc} = 350 nm) spectra of 5 wt% Y_2O_3:$Dy_{0.0085}$ NPs / α-Al_2O_3 recorded between 28.6 and 600 °C in steps of 50 °C. (b): Logplot of the fluorescence intensity ratio (FIR) versus T^{-1} between 28.6 and 600 °C. The intensity ratio was calculated by dividing the integrated area between 440-471 nm and 571-510 nm of the emission spectra.

Further investigation of the temperature-dependent luminescence was done by calculating the natural logarithm of the fluorescence intensity ratio (FIR) and plotting the results versus 1/*T*, see Figure 3-16 (b). However, no linear trend could be observed over a broad temperature range which is expected from the thermal coupling of the $^4I_{15/2}$ and $^4F_{9/2}$ populations. The reason for this absence is an insufficient signal to noise ratio. This makes this system unsuitable for temperature probing by exploiting the temperature dependent emission.

As discussed previously, the low signal to noise ratio arises by the scattering of α-Al_2O_3 since the excitation wavelength is close to the emission. In this system, the scattering appears since the Y_2O_3Ln NPs are deposited on α-Al_2O_3. Since scattering is dependent of the size of particles, similar experiments were performed to investigate the scattering of Y_2O_3:$Dy_{0.0085}$ NPs without α-Al_2O_3. It is expected that scattering is absent solely Y_2O_3:$Dy_{0.0085}$ NPs.

Figure 3-17 shows the emission spectra upon excitation at 350 nm between room temperature (blue) and 600 °C (red) in steps of 25 °C. The signal to noise ratio is significantly higher and the declining background is absent in comparison to the sample of 5 wt% Y_2O_3:$Dy_{0.0085}$ NPs / α-Al_2O_3. Furthermore, it is obvious that with increasing temperature the $^4F_{9/2}\rightarrow{}^6H_{15/2}$ emission decreases whereas the $^4I_{15/2}\rightarrow{}^6H_{15/2}$ emission is enhanced, suggesting the thermal coupling of the $^4F_{9/2}$, $^4I_{15/2}$ energy levels.

The temperature-dependent luminescence was further investigated by calculating the natural logarithm of the FIR and plotting the results versus the inverse of the temperature, shown in Figure 3-18. The experimental data between 100 and 600 °C was fitted to a linear model. The coefficient of determination (R^2) was found to be 0.9958 which implies that the model fit represents the experimental data good. The linear dependence between 100 and 600 °C makes the Y_2O_3:$Dy_{0.0085}$ NPs suitable for temperature probing within this temperature region. The energy difference from the $^4I_{15/2}$ and $^4I_{15/2}$ energy levels was found to be 935 cm^{-1} from the slope of the linear fit. This value agrees with the energy difference deduced from the Dieke diagram which is approximately 1000 cm^{-1}.[3]

Thermal cycling experiments were carried out to study the durability and accuracy of the Y_2O_3:$Dy_{0.0085}$ NPs as temperature probes. Figure 3-19 (a) and (b) show respectively the obtained emission spectra and calculated temperatures from the spectra using the linear fit determined in Figure 3-18. As can be seen, the spectra overlap during cycling what confirms the preservation of luminescence. Furthermore, the accuracy was determined by calculating the standard deviation at each temperature. Accuracies of 7.2, 5.0, 6.2, 7.0 and 14.2 °C were found for the spectra obtained 100, 225, 350, 475 and 600 °C, respectively. The relatively low accuracies are ascribed to the low signal to noise ratios in the emission spectra.

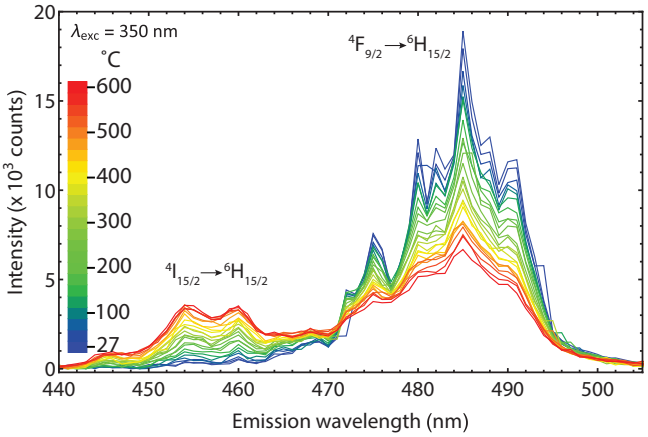

Figure 3-17: Emission (λ_{exc} = 350 nm) spectra of Y_2O_3:$Dy_{0.0085}$ NPs recorded between 28.6 and 600 °C in steps of 25 °C.

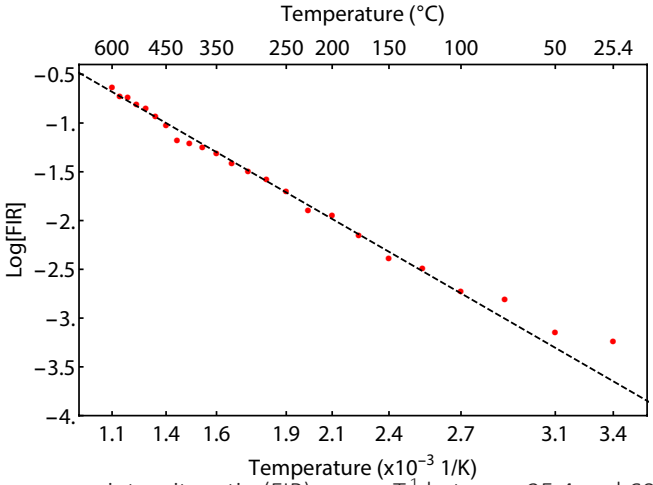

Figure 3-18: Logplot of the fluorescence intensity ratio (FIR) versus T^{-1} between 25.4 and 600 °C. The intensity ratio was calculated from the emission spectra by dividing the integrated area between 440-471 nm and 471-510 nm. The linear model was fitted between 100 and 600 °C with a calculated coefficient of determination (R^2) of 0.9958.

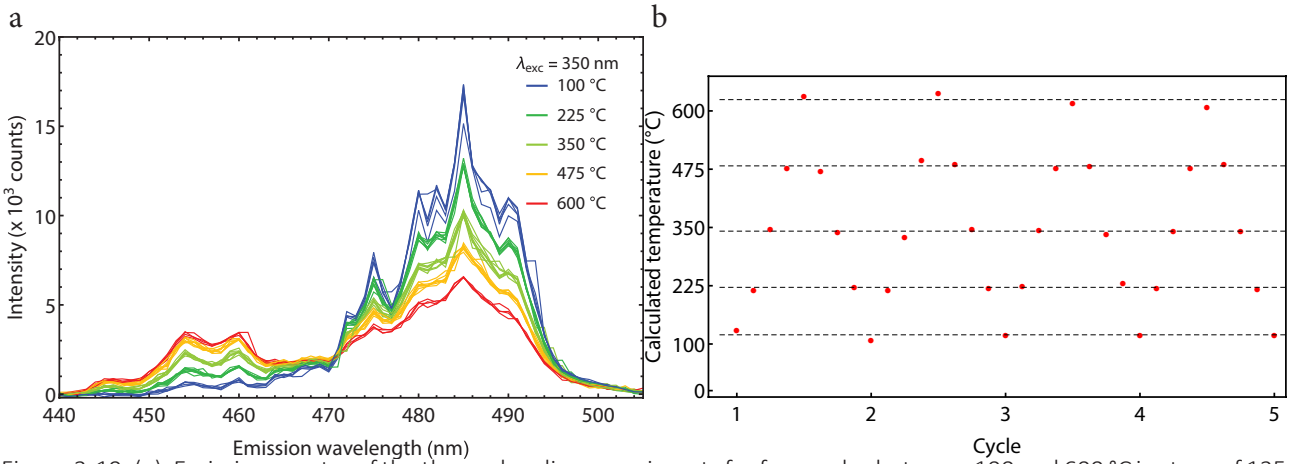

Figure 3-19: (a): Emission spectra of the thermal cycling experiments for four cycles between 100 and 600 °C in steps of 125 °C. (b): Calculated temperatures from the thermal cycling experiment by exploiting the emission spectra and the model fit.

5. Optimal dopant concentrations for the temperature dependent luminescence of $Y_2O_3:Er_x$-Yb_y NPs

Erbium emits green (520 - 570 nm) and red (645 - 690 nm) light in the visible spectrum from the $^2H_{11/2}$, $^4S_{3/2}\rightarrow{}^4I_{15/2}$ and $^4F_{9/2}\rightarrow{}^4I_{15/2}$ transitions, respectively. Previous research has shown that the green and red emission is determined by the dopant concentrations of erbium and ytterbium ions.[8] Since the temperature dependent emission lies in the green emission region, it is required to maximize the luminescence of the $^2H_{11/2}$, $^4S_{3/2}\rightarrow{}^4I_{15/2}$ transitions. Therefore, various samples were made containing $Y_2O_3:Er_{0.02}$ NPs, $Y_2O_3:Er_{0.02}Yb_{0.05}$ NPs, $Y_2O_3:Er_{0.01}Yb_{0.01}$ NPs and $Y_2O_3:Er_{0.001}Yb_{0.01}$ NPs to investigate the optimal intensity of the $^2H_{11/2}$, $^4S_{3/2}\rightarrow{}^4I_{15/2}$ transitions. The samples were excited with a 2W laser at 980 nm to study the upconversion spectra. The results are shown in Figure 4-13 for $Y_2O_3:Er_{0.01}Yb_{0.01}$ NPs and in Appendix 3.7.2 for the additional samples. It was found that the sample with $Y_2O_3:Er_{0.01}Yb_{0.01}$ NPs showed the highest emission intensity of the $^2H_{11/2}$, $^4S_{3/2}\rightarrow{}^4I_{15/2}$ transitions.

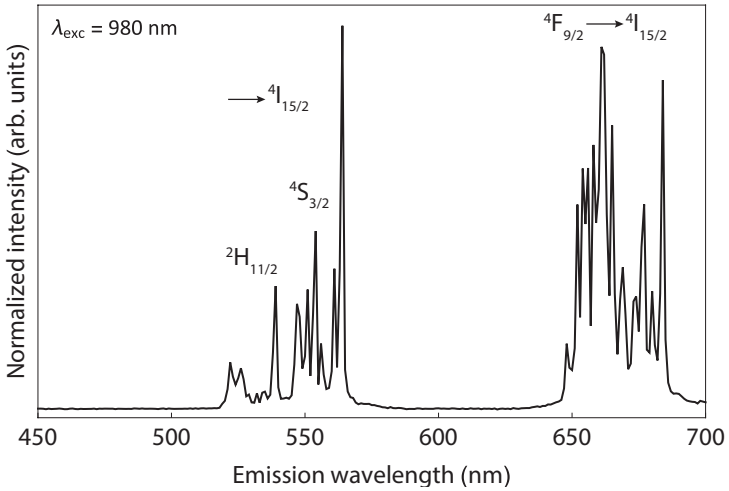

Figure 3-20: Upconversion spectra of $Y_2O_3:Er_{0.01}Yb_{0.01}$ NPs recorded at room temperature upon excitation with a 2 W laser at 980 nm.

6. Temperature dependent luminescence of Y_2O_3:$Er_{0.01}Yb_{0.01}$ /α-Al_2O_3

To determine the temperature dependent luminescence of Y_2O_3:$Er_{0.01}Yb_{0.01}$ NPs, upconversion spectra were recorded of 5 wt% Y_2O_3:$Er_{0.01}Yb_{0.01}$ NPs / α-Al_2O_3 between 27 and 600 °C upon excitation with a 2 W laser at 980 nm. Figure 3-21 (a) shows the unnormalized spectra in the wavelength range from 500 up to 580 nm. The position of the peaks is preserved although the ratio increases with increasing temperature due to multi-phonon relaxation. Even though the intensity decreases, it is sufficient to determine the fluorescence intensity ratio from the $^2H_{11/2}\rightarrow{}^4I_{15/2}$ and $^4S_{3/2}\rightarrow{}^4I_{15/2}$ transitions. Figure 3-21 (b) shows the upconversion spectra normalized at the emission peak of 563 nm to visualize the temperature dependence. As can be seen, the $^2H_{11/2}\rightarrow{}^4I_{15/2}$ versus $^4S_{3/2}\rightarrow{}^4I_{15/2}$ ratio increases with increasing temperature as expected from the thermal coupling of the $^2H_{11/2}$ and $^4S_{3/2}$ excited states.

To investigate the temperature dependence more in-depth, the natural logarithm of the calculated fluorescent intensity ratio from every spectrum versus the inverse of the temperature was plotted, shown in Figure 3-22. The data points between room temperature and 500 °C show a linear dependence, as expected from Equation 3-6. Therefore, the experimental data between 27.2 and 500 °C was fitted to a linear model. The experimental data points above 500 °C are not taken into account since there is a strong deviation from the fit. The coefficient of determination (R^2) of the linear model was found to be 0.9995, *i.e.* the model fit corresponds good with the experimental data.

The decrease in luminescence above 475 °C results in an insufficient signal to noise ratio for temperature probing. This is also visible in Figure 4-21 (b) where the spectra above 500 °C become noisy. Therefore, this system is suitable for temperature probing between room temperature and 500 °C. From the slope of the fit the energy difference ΔE between the thermally coupled levels $^2H_{11/2}$ and $^4S_{3/2}$ can be calculated which was found to 879 cm^{-1}. This value is in the same order of magnitude as from the Dieke diagram which is approximately 750 cm^{-1}.[3]

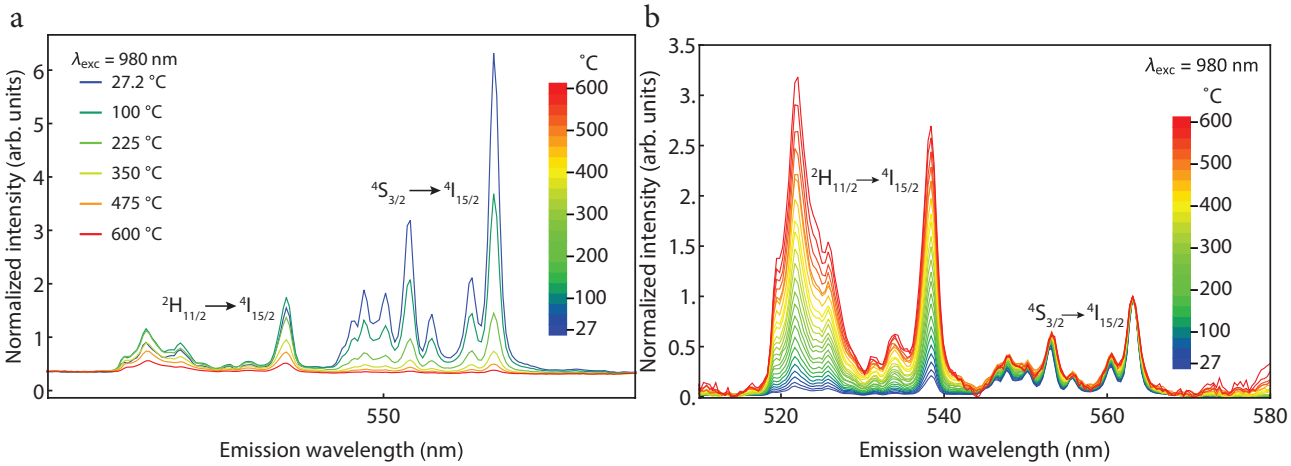

Figure 3-21: Temperature dependent upconversion spectra of 5 wt% Y_2O_3:$Er_{0.01}Yb_{0.01}$ / α-Al_2O_3. (a) Unnormalized spectra recorded between 27.2 and 600 °C. (b): Spectra normalized at 563 nm between 27.2 and 600 °C in steps of 25 °C.

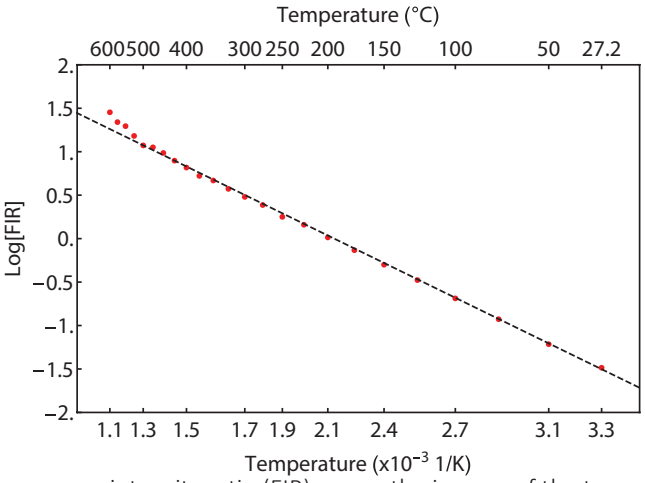

Figure 3-22: Logplot of the fluorescence intensity ratio (FIR) versus the inverse of the temperature between 27.2 and 600 °C. Linear fit is between 27.2 and 500 °C with R^2 = 0.9995.

7. Thermal cycling measurements

The final application requires durable and accurate temperature probes. Thermal cycling experiments were carried out with the 5 wt% Y_2O_3:$Er_{0.01}Yb_{0.01}$ NPs / α-Al_2O_3 to investigate these characteristics. Four temperature cycles were performed between 100 and 475 °C while measuring the emission spectra at 100, 225, 350 and 475 °C. Figure 3-23 (a) shows the spectra normalized on the maximum intensity of the $^4S_{3/2}\rightarrow{}^4I_{15/2}$ emission peak. The spectra overlap during the heating and cooling cycles what indicates that the temperature dependent emission is preserved. Figure 3-23 (b) shows the calculated temperatures from the intensity ratios of the emission spectra, by exploiting the model fit of Figure 3-22. The dashed lines indicate average values of the calculated temperatures during. The cycles show identical trends and the calculated temperatures do not change significant during cycling, suggesting durable and accurate temperature probes. Nevertheless, the calculated temperatures at 475 °C deviate approximately 10 °C of the set temperature. A possible explanation for this is that the measurements are performed at the upper bound of the model fit and are therefore less accurate.

The accuracy of the temperature probes was determined by calculating the standard deviations in temperature from the cycling experiments. Accuracies of 0.7, 0.8, 1.7 and 2.8 °C were found for the temperature measurements performed at 100, 225, 350 and 475 °C, respectively. Compared to the 5 wt% Y_2O_3:$Eu_{0.05}$ NPs / α-Al_2O_3 and Y_2O_3:$Dy_{0.0085}$ NPs samples, the accuracy of 5 wt% Y_2O_3:$Er_{0.01}Yb_{0.01}$ NPs / α-Al_2O_3 is rather high. The emission intensity of the Y_2O_3:$Er_{0.01}Yb_{0.01}$ NPs / α-Al_2O_3 temperature probes is high and the change in luminescence of $^2H_{11/2}$,$^4S_{3/2}\rightarrow{}^4I_{15/2}$ transitions with increasing temperature is relatively large, yielding an excellent system for temperature probing.

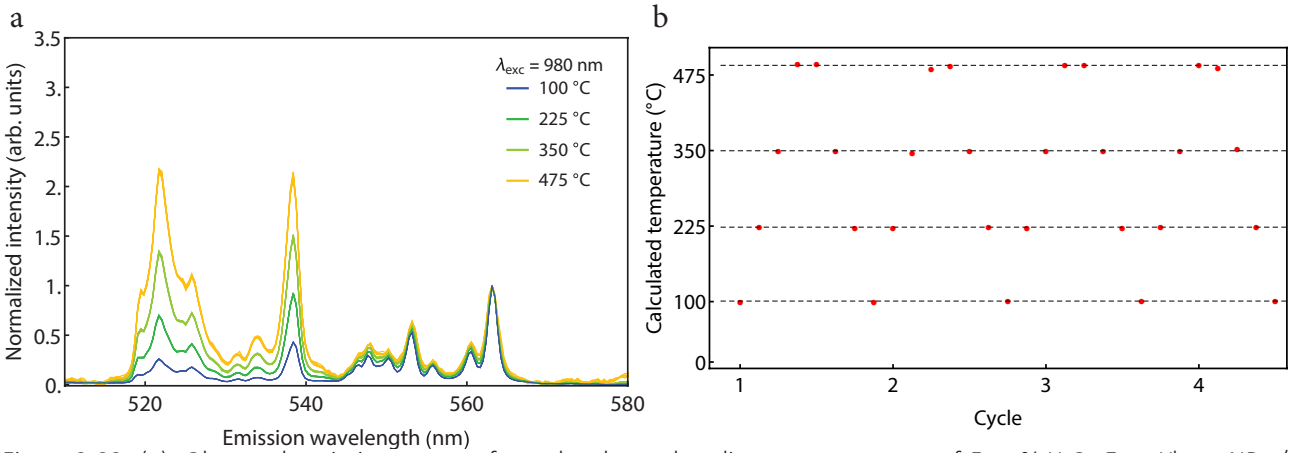

Figure 3-23: (a): Observed emission spectra from the thermal cycling measurements of 5 wt% Y_2O_3:$Er_{0.01}Yb_{0.01}$ NPs / α-Al_2O_3 at temperatures of 100, 225, 350 and 475 °C, normalized at 563 nm. (b): Calculated temperature for every spectrum by exploiting the fluorescence intensity ratio. The dashed lines indicate the average calculated temperature.

3.5 Conclusion

In this chapter, the temperature dependent luminescence of Eu^{3+}-, Dy^{3+}- and Er^{3+}/Yb^{3+}-doped Y_2O_3 NPs on α-Al_2O_3 was investigated. It was found that $Y_2O_3:Eu_{0.05}$ NPs / α-Al_2O_3 exhibit temperature dependent emission from the $^5D_{0,1}\rightarrow{}^7F_J$ transitions between 530 and 640 nm. A workable range between 225 and 600 °C was determined emission intensity from the $^5D_1\rightarrow{}^7F_J$ transitions below 225 °C was not observable. We were not able to deduce a temperature dependence from $Y_2O_3:Dy_{0.0085}$ NPs / α-Al_2O_3 of the $^4I_{15/2}\rightarrow{}^6H_{15/2}$ and $^4F_{9/2}\rightarrow{}^6H_{15/2}$ transitions because the signal to noise ratio was too low. Therefore, undeposited bare $Y_2O_3:Dy_{0.0085}$ NPs were investigated and a temperature dependence from 100 °C up to 600 °C was observed. Upconversion luminescence of $Y_2O_3:Er_{0.01}Yb_{0.01}$ NPs / α-Al_2O_3 revealed the presence of a temperature dependence from the $^2H_{11/2}$, $^4S_{3/2}\rightarrow{}^4I_{15/2}$ transitions from room temperature up to 500 °C.

Thermal cycling experiments were carried out for $Y_2O_3:Eu_{0.05}$ NPs / α-Al_2O_3, $Y_2O_3:Dy_{0.0085}$ NPs and $Y_2O_3:Er_{0.01}Yb_{0.01}$ NPs / α-Al_2O_3 complexes to investigate the durability and accuracy of the temperature probes. All systems have shown to remain their luminescence during the thermal cycles. The accuracy was relatively low for the $Y_2O_3:Eu_{0.05}$ NPs / α-Al_2O_3, $Y_2O_3:Dy_{0.0085}$ NPs systems by low emission intensity, resulting in accuracies between 5.0 and 14.2 °C. The $Y_2O_3:Er_{0.01}Yb_{0.01}$ NPs / α-Al_2O_3 showed a higher accuracy from 0.7 up to 2.8 °C.

3.6 References

[1] S. Cotton. Lanthanide and Actinide Chemistry. *John Wiley & Sons*, 2006.

[2] G. Blasse and B.C. Grabmaier. Luminescent materials. *Springer-Verlag*, 1994.

[3] G.H. Dieke, Spectra and energy levels of rare earth ions in crystals. *Interscience Publishers*, 1968.

[4] R. Wegh, A. Meijerink, R. Lamminmäki and J. Hölsä. Extending Dieke's diagram. *Journal of Luminescence*, 89:1002–1004, 2000.

[5] P.A. Tanner, Some misconceptions concerning the electronic spectra of tri-positive europium and cerium. *Chemical Society Reviews*, 42:5090-5101, 2013.

[6] F. Vetrone, J. Boyer, J.A. Capobianco, A. Speghini and M. Bettinelli. Significance of Yb^{3+} concentration on the upconversion mechanisms in codoped Y_2O_3:Er^{3+}, Yb^{3+} nanocrystals. *Journal of applied physics*, 96:661-667 2004.

[7] S.K. Singh, K. Kumar and S.B. Rai. Er^{3+}/Yb^{3+} codoped Gd_2O_3 nano-phosphor for optical thermometry. *Sensors and Actuators A*, 149:16-20, 2009.

[8] D. Matsuura. Red, green, and blue upconversion luminescence of trivalent-rare-earth ion-doped Y_2O_3 nanocrystals. *Applied Physics Letters 81*, 24:4256-4528.

[9] H. Guo, N. Dong, M. Yin, W. Zhang, L. Lou and S. Xia. Visible upconversion in rare earth ion-doped Gd_2O_3 nanocrystals. *Journal Physical Chemistry B*, 108:19205-19209, 2004.

[10] H. Kusuma, O.J. Sovers and T. Yoshioka. Line shift method for phosphor temperature measurements. *Japanese Journal of Applied Physics*, 15:2349-2358, 1976.

[11] Y. Kumar, M. Pal, M. Herrera and X. Mathew. Effect of Eu ion incorporation on the emission behavior of Y_2O_3 nanophosphors: A detailed study of structural and optical properties. *Optical materials*, 60:159-168, 2016.

[12] G. Dominiak-Dzik, W. Ryba-Romanowski, L. Kovács and E. Beregi. Effect of temperature on luminescence and VUV to visible conversion in the $YAl_3(BO_3)_4$:Dy^{3+} (YAB:Dy) crystal. *Radiation Measurements*, 38:557-561, 2004.

[13] Z. Boruc, M. Kaczkan, B. Fetlinski, S. Turczynski and M. Malinowski. Blue emissions in Dy^{3+} doped $Y_4Al_2O_9$ crystals for temperature sensing. *Optics Letters 37*, 24:5214-5216.

3.7 Appendix

1. Excitation and emission spectra of Y_2O_3:$Dy_{0.0085}$ NPs / α-Al_2O_3 complexes

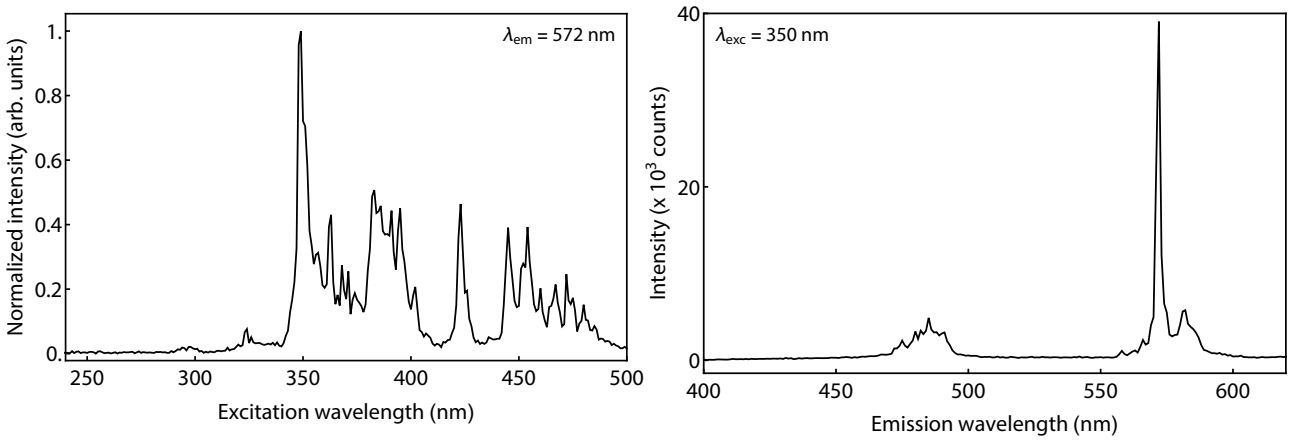

Figure 3-24: Excitation (λ_{em} = 572 nm) and emission (λ_{exc} = 350 nm) spectra of 5 wt% Y_2O_3:$Dy_{0.0085}$ NPs / α-Al_2O_3 recorded at room temperature.

2. Optimal dopant concentrations of Y_2O_3:Er_xYb_y NPs

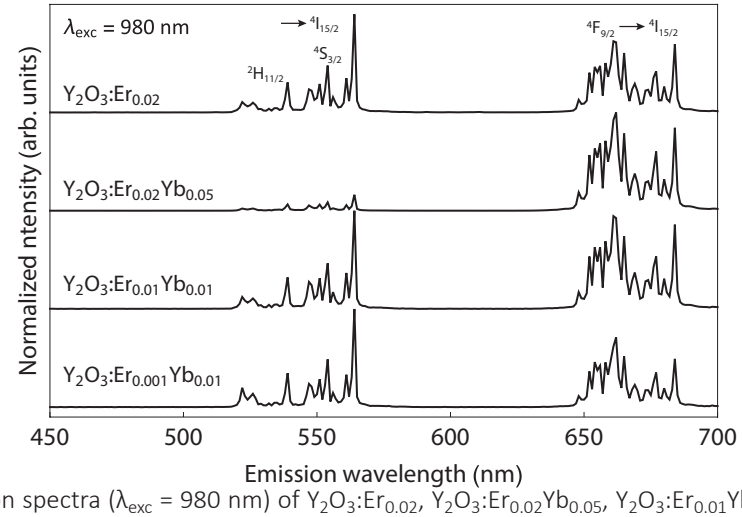

Figure 3-25: Upconversion spectra (λ_{exc} = 980 nm) of Y_2O_3:$Er_{0.02}$, Y_2O_3:$Er_{0.02}Yb_{0.05}$, Y_2O_3:$Er_{0.01}Yb_{0.01}$ and Y_2O_3:$Er_{0.001}Yb_{0.01}$ NPs recorded at room temperature.

3. Excitation and emission spectra of Y_2O_3:$Er_{0.01}Yb_{0.01}$ NPs

Excitation and emission spectra of Y_2O_3:$Er_{0.01}Yb_{0.01}$ NPs were recorded to study the influence of the excitation wavelength on the green and red emission of the NPs. The results are depicted in Figure 4-15. Excitation spectra (λ_{em} = 564 and 661 nm) show sharp lines at 379 and and 488 nm originating from the $^4I_{15/2} \rightarrow {}^4G_{7/2,\ 11/2}$ and $^4I_{15/2} \rightarrow {}^4F_{7/2}$ f-f transitions.

The emission spectra of the sample under excitation of 379 and 488 nm show the characteristic $^2H_{11/2}$, $^4S_{3/2} \rightarrow {}^4I_{15/2}$ green emission while the red $^4F_{9/2} \rightarrow {}^4I_{15/2}$ emission is absent. The red emission is not present since the energy gap between the $^4S_{3/2}$ and $^4F_{9/2}$ energy levels ($\Delta E = 3200\ cm^{-1}$) is too large to be bridged by multi-phonon relaxation. Furthermore, in the emission spectrum of λ_{exc} = 488 nm a decreasing background between 500 and 570 nm exists what originates from scattering effects. This phenomon is absent when the sample is excited at 379 nm because of the larger separation between the excitation and emission wavelengths.

When we compare above results the optimal excitation wavelengths for observing the temperature dependent $^2H_{11/2}$, $^4S_{3/2} \rightarrow {}^4I_{15/2}$ emission are 379 and 980 nm. Excitation at a wavelength of 488 nm is unsuitable since scattering effects overlap with the temperature dependent $^2H_{11/2}$, $^4S_{3/2} \rightarrow {}^4I_{15/2}$ emission. Excitation of the sample at 980 nm is favoured over 379 nm since it has a longer penetration depth and exhibits a higher emission intesity. Therefore, temperature dependent measurements were done under excitation of 980 nm.

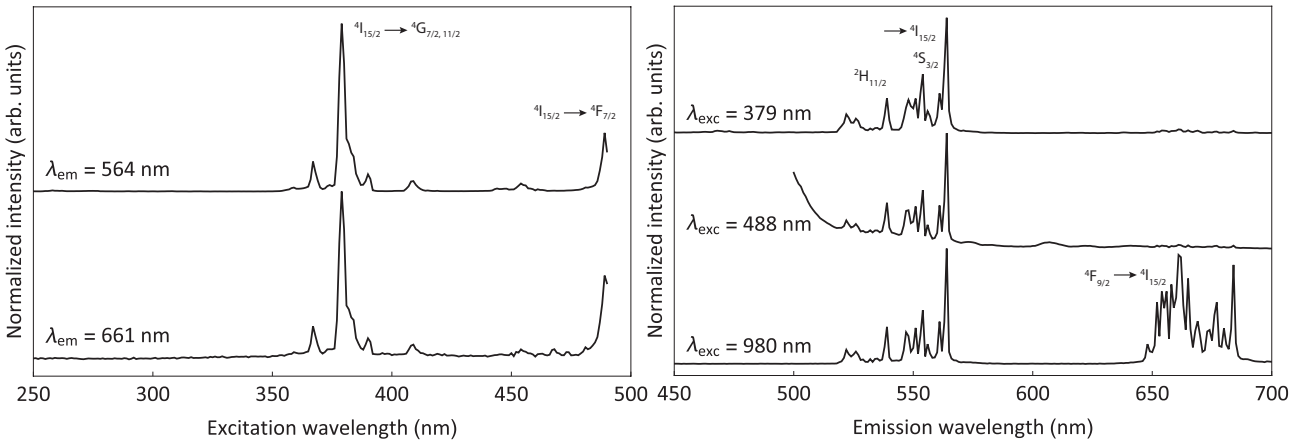

Figure 3-26: Excitation (λ_{em} = 564 and 661 nm) and emission (λ_{exc} = 379, 488 and 980 nm) spectra of Y_2O_3:$Er_{0.01}Yb_{0.01}$ NPs recorded at room temperature. Excitation took place with a Xe lamp excepting 980 nm what was done with a diode laser.

Conclusion

The main purpose of this work was to develop luminescent temperature probes for *in situ* temperature measurements in catalytic environments at high temperatures. Luminescent Y_2O_3:Ln NPs / α-Al_2O_3 (Ln = Eu^{3+}, Dy^{3+} or Er^{3+}/Yb^{3+}) complexes were synthesized via the deposition of Y_2O_3:Ln NPs on α-Al_2O_3. The preparation of Y_2O_3:Ln NPs by homogeneous precipitation generated Ln-doped NPs between 50 and 250 nm in size. The deposition of the Ln-doped Y_2O_3 NPs on α-Al_2O_3 yielded thermally and mechanically stable complexes that were tested for behaviour in temperature dependent luminescence. It was found that Eu^{3+} and Er^{3+}/Yb^{3+}-doped complexes showed temperature dependent emission in the temperature ranges of 225-600 °C and 22-500 °C, respectively. Although temperature dependent emission of Dy^{3+}-doped complexes was observed, the signal to noise ratio was unsufficient for temperature measurements. To examine the accuracy of the Eu^{3+} and Er^{3+}/Yb^{3+}-doped temperature probes, thermal cycling experiments were perfomed between room temperature and 600 °C. The temperature dependent luminescence remained unaltered during multiple cycles. Accuracies higher than 14.2 and 2.8 °C were found for the Eu^{3+} and Er^{3+}/Yb^{3+} complexes, respectively.

An extensive toolbox of Y_2O_3:Ln NPs / α-Al_2O_3 has been developed for temperature probing between room temperature up to 600 °C with a high accuracy. The reported temperature probes are promising candidates for luminescent temperature probing in catalytic environments.

Future research

1. Investigation of the temperature probes under representative catalytic conditions

So far, the Y_2O_3:Ln / α-Al_2O_3 complexes have been synthesized and characterized but not studied under relevant conditions. The next step in the reseach towards temperature probes is to test the performance of the temperature probes during a catalytic reaction. Figure 4-1 shows a schematic representation for a set-up to investigate the performance at unexplored conditions.

Catalytically active NPs will be deposited on α-Al_2O_3 next to the Y_2O_3:Ln temperature probes. It is favourable to use Y_2O_3:Er^{3+}/Yb^{3+} temperature probes since a high emission intensity was observed. The excitation of the NPs in the IR leads to relatively deep penetration depths in the liquid phase. A glass or quartz window in the reactor wall is required to illuminate and detect emission from the temperature probes. To start relatively easy, it is preferred to probe a temperature gradient instead of an uniform temperature, the mobile phase and the catalytic active NPs should be chosen such that an exothermic reaction will be performed. Heat will be generated by the chemical conversions what will result in a temperature gradient over the mobile phase. By moving the excitation source and detector over the glass window the temperature in the reactor can be probed.

A possible side effect that has to be investigated is the interference of rare earths with the catalytic reaction. Numerous studies can be found in literature were cerium and other rare earth are used as promotors in catalytic reactions.[1-3] Therefore, it is essential to investigate side effects of the rare earth metals on the catalytic performance.

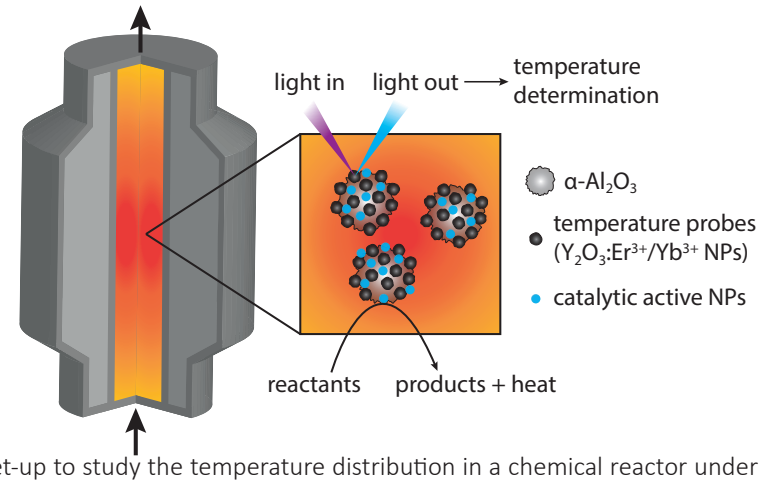

Figure 4-1: Proposed set-up to study the temperature distribution in a chemical reactor under industrial conditions. The stream flows from bottom to top while exothermic reactions generate a temperature gradient over the mobile phase. The temperature will be probed by the temperature dependent luminescence from the Y_2O_3:Ln NPs through a glass window.

2. Luminescence

Although Y_2O_3:$Eu_{0.05}$ complexes NPs exhibit temperature dependent emission, the temperature dependence below 225 °C is not understood. It is thought that the temperature dependent multi-phonon relaxation plays an important role, but no proof has been given. Decay measurements could help to reveal the nature of this dependence.

Another aspect that has to be improved is the luminescence of the Y_2O_3:$Dy_{0.0085}$ NPs. Though Y_2O_3:$Dy_{0.0085}$ NPs show temperature dependent emission, the signal to noise ratio is insufficient for temperature probing when deposited on α-Al_2O_3. A first suggestion to enhance the luminescence is the usage of Gd_2O_3 instead of Y_2O_3 as host material. Gadolinium (Gd^{3+}) exhibits a strong absorption band at 273 nm by intraconfigurational $4f^n$ - $4f^n$ transitions and transfers its energy to dysprosium.[4] Furthermore, the synthesis of co-doped Gd_2O_3 NPs by homogeneous precipitation is similar to those of Y_2O_3 NPs and is reported in literature.[5,6]

A second suggestion is the usage of Ce^{3+} for the sensitization of dysprosium. Cerium exhibits a strong absorption band in the UV by a 4f-5d transition. Currently, this ion is used for the activation of lumi-

nescent lanthanide ions in host materials such as YAG and $LaPO_4$.[7] However, it has been shown that cerium is unsuitable for sensitizing activators in Y_2O_3 since the energy is quenched by the relatively low-lying conduction band of Y_2O_3.[8,9] Therefore, cerium has to be incorporated in alternative host materials such as Gd_2O_3, yielding $Gd_2O_3:Dy_xCe_y$ where cerium acts as activator for dysprosium.

When embedded in a catalytic reactor, catalysts are subject to the formation of coke and/or other species on the surface what changes the colour of the material.[10] Since the temperature is deduced from the luminescence of the Y_2O_3:Ln NPs / α-Al_2O_3 complexes, it is of high importance to examine the effect of the colour change on the temperature determination.

3. References

[1] A. Trovarelli, C. de Leitenburg, M. Boaro and G. Dolcetti. The utilization of ceria in industrial catalysis. *Catalysis Today*, 50:353-367, 1999.

[2] F. Wang and G. Lu. High performance rare earth oxides LnO_x (Ln = La, Ce, Nd, Sm and Dy)-modified Pt/SiO_2 catalysts for CO oxidation in the presence of H_2. *Journal of Power Sources*, 181:120-126, 2008.

[3] H. Huang, N. Young, B.P. Williams, S.H. Taylor and H. Hutchings. Purification of chemical feedstocks by the removal of aerial carbonyl sulfide by hydrolysis using rare earth promoted alumina catalysts. *Green Chemistry*, 10:571-577, 2008.

[4] S. Majeed and S.A. Shivashankar. Microspherical, hierarchical structures of blue-green-emitting Dy:GdOOH and Dy:Gd_2O_3. *Materials Letters*, 125:136-139, 2014.

[5] E. Matijevic and W.P. Hsu. Preparation and properties of monodispersed colloidal particles of lanthanide compounds. *Journal of Interface and Colloid Science*, 118:506-523, 1987.

[6] S. Gai, P. Yang, D. Wang, C. Li, N. Niu, F. Hea and X. Li. Monodisperse Gd_2O_3:Ln (Ln=Eu^{3+}, Tb^{3+}, Dy^{3+}, Sm^{3+}, Yb^{3+}/Er^{3+}, Yb^{3+}/Tm^{3+}, and Yb^{3+}/Ho^{3+}) nanocrystals with tunable size and multicolor luminescent properties. *CrystEngComm*, 13:5480-5487, 2011.

[7] G. Blasse and B.C. Grabmaier. Luminescent materials. *Springer-Verlag*, 1994.

[8] M. Raukas, S.A. Basum, W. van Schaik, W.M. Yen and U. Happek. Luminescence efficiency of cerium doped insulators: The role of electron transfer processes. *Applied Physics Letters 69*, 22:3300-3302.

[9] M. Raukas, S. Basun, W.M. Dennis, D.R. Evans, U. Happek, W. van Schaik and W.M. Yen. Optical properties of Ce^{3+}-doped Lu_2O_3 and Y_2O_3 single cexarystals. *Journal for the Society for Information Display*, 4/3, 1996.

[10] M.D. Argyle and C.H. Bartholomew. Heterogeneous catalyst deactivation and regeneration: A review. *Catalysts*, 5:145-269, 2015.

Acknowledgements

The work of this thesis was made possible with the help of a number of people whose effort I would like to acknowledge.

First of all, I would like to thank both Robin and Anne-Eva for their daily supervision. From the beginning of my project you were enthusiastic and helpful to me. You helped me a lot and remained positive, even when my findings were not in line with our expectations. And although I was not familiar with the ICC group when I started my thesis, Anne-Eva helped me to find my way there. I have learned a lot from both of you and you really helped me to develop my scientific skills.

Secondly, I would like to thank Andries for his general supervision over my project. Thank you for giving me the opportunity to do my master thesis in the CMI and ICC groups. Your door was always open to discuss my findings and you gave useful answers and advice.

Thirdly, I would like to thank my fellow bachelor and master students from both CMI and ICC for their support during my research. You helped me a lot, either with fixing bugs in mathematica scripts, using measurement set-ups or by giving me advice for the best presentation of my data. For me it felt as a fruitful atmosphere where we have learned a lot from each other.

Fourthly, I would like to thank the remaining people of both research groups for helping me. I experienced both groups as very open and helpful. In summary, I have had a great time and enjoyed it very much!